American Mineralogist, Volume 91, pages 1271–1292, 2006

Single-crystal X-ray diffraction and temperature dependent ^{57}Fe Mössbauer spectroscopy on the hedenbergite-aegirine $(Ca,Na)(Fe^{2+},Fe^{3+})Si_2O_6$ solid solution

GÜNTHER J. REDHAMMER,[1,2,*] GEORG AMTHAUER,[1] GEORG ROTH,[2] GEROLD TIPPELT,[1] AND WERNER LOTTERMOSER[1]

[1]Department of Material Science, Division of Mineralogy, University Salzburg, Hellbrunnerstr. 34, A-5020, Salzburg, Austria
[2]Institute of Crystallography, University of Technology, Rheinisch—Westfälische Technische Hochschule Aachen, Jägerstrasse 17/19, D-52056, Aachen, Germany

ABSTRACT

Synthetic samples with different chemical compositions along the hedenbergite–aegirine ($CaFe^{2+}Si_2O_6$–$NaFe^{3+}Si_2O_6$) solid-solution series have been investigated by single-crystal X-ray diffraction and ^{57}Fe Mössbauer spectroscopy. All compounds show *C*2/*c* symmetry, both at 298 K and at low temperature (100 K). The structural changes within the hedenbergite–aegirine series are dominated by the M1 site while the M2 site plays a minor role. Replacement of Fe^{2+} by Fe^{3+} increases the polyhedral distortion of the M1 site and causes an increased repulsion between neighboring M1 sites. The changes in M1-site geometry also induce distinct alterations within the kinking state of the tetrahedral chains, but the changes in tetrahedral bond lengths and angles are small. In addition to the single-crystal X-ray diffraction experiments, a large number of synthetic samples were investigated by ^{57}Fe Mössbauer spectroscopy at 298 K and, for three selected compositions, between 80 and 700 K. Here, substantial line broadening of the Fe^{2+} resonance absorption was observed as an aegirine component is substituted. Two different groups of local distortion environments were observed for Fe^{2+} within the solid-solution series, which change relative proportions and numeric value of the quadrupole splitting as a function of chemistry and temperature. This line broadening cannot be ascribed to discrete next-nearest-neighbor (NNN) configurations of Ca and Na as has been done in the literature. Above ~250 K, additional resonance absorption appears in the spectra of samples with aegirine components between 20 and 75 mol%. This absorption gains intensity with increasing temperature, while the ^{57}Fe hyperfine parameters approach values intermediate between Fe^{2+} and Fe^{3+}. This effect is ascribed to fast electron delocalization between Fe^{2+} and Fe^{3+} at elevated temperature.

Keywords: Synthesis, crystal structure, Mössbauer spectroscopy, hedenbergite–aegirine series, clinopyroxenes

INTRODUCTION

Both hedenbergite ($CaFe^{2+}Si_2O_6$) and aegirine ($NaFe^{3+}Si_2O_6$) are clinopyroxenes that are monoclinic with *C*2/*c* symmetry at room temperature (Clark et al. 1969; Cameron et al. 1973; Redhammer et al. 2000). A topological description and representations of the crystal structure of clinopyroxenes including the atomic nomenclature of Burnham et al. (1967) can be found elsewhere (e.g., Cameron and Papike 1981; Redhammer et al. 2000) and will not be repeated here.

Both end-members have been investigated structurally several times. Redhammer et al. (2000) were the first to give structural data for synthetic samples on this join. They refined the crystal structures of 7 different compositions of the hedenbergite–aegirine solid-solution series by means of the Rietveld method from powder data. However, they were not able to extract detailed information on structural changes (variation of individual bond lengths, bond angles, distortion parameters) as a function of chemical composition. Furthermore, information on the low-temperature crystal structure is not yet available. This information, however, is of basic importance for understanding and interpreting trends in ^{57}Fe hyperfine parameters as derived from Mössbauer spectroscopy. Also, atomic positional parameters are the basic input data for any theoretical calculation of the electronic structure of the clinopyroxenes under investigation.

^{57}Fe Mössbauer spectroscopy has been applied in several instances to the study of clinopyroxenes (Bancroft and Williams 1969; Aldridge et al. 1978; Williams et al. 1971). Dollase and Gustafson (1982) investigated 4 different synthetic samples of the hedenbergite–aegirine solid-solution series by Mössbauer spectroscopy at 77 and 298 K and found substantial, *asymmetric* Fe^{2+} resonance absorption line broadening. Similar observations were made by Aldridge et al. (1978) for a natural *C*2/*c* omphacite and by Amthauer and Rossman (1984) for a natural aegirine. Two opposing interpretations have been given for this behavior. Aldridge et al. (1978) assigned this effect to next-nearest-neighbor (NNN) influences arising from different occupation of the M2 site by Ca^{2+} and Na^{+}, respectively. This interpretation also was favored by Dowty and Lindsley (1973) to explain Fe^{2+} line broadening along the hedenbergite–ferrosilite $Fe_2Si_2O_6$ solid solution. In contrast, Amthauer and Rossman (1984) suggested that an inner Fe^{2+} doublet arises from thermally activated electron charge transfer between Fe^{2+} and Fe^{3+}, whereas the outer Fe^{2+} doublet was assigned to pure ionic Fe^{2+} on the M1 site. Dollase

* E-mail: guenther.redhammer@sbg.ac.at

0003-004X/06/0809–1271$05.00/DOI: 10.2138/am.2006.2173

and Gustafson (1982) as well as De Grave et al. (1998), who investigated a natural aegirine sample, stated that neither interpretation could be considered conclusive. Recently, Eeckhout and De Grave (2003a, 2003b) studied in detail the paramagnetic and magnetic Mössbauer spectra of two natural Mg-containing hedenbergite samples.

As exact structural data obtained from single crystals are of major importance for any detailed crystal-chemical discussion of the system and for the interpretation of the ^{57}Fe Mössbauer data, the aim of the present study was to first find ways to synthesize single crystals of samples along the hedenbergite–aegirine join and to refine their crystal structure to high precision. This approach should enable us to arrive at a deeper understanding of the structural changes accompanying substitution of $Ca^{2+}Fe^{2+}$ by $Na^{+}Fe^{3+}$. The second major objective of the present study was to contribute new facts and possible interpretations for the asymmetric Fe^{2+} line broadening by recording Mössbauer spectra on selected compositions in a wide temperature range. A Voigt-function-based quadrupole splitting distribution (QSD) method (Rancourt and Ping 1991) was applied to refine the spectra and to extract QSDs as a function of temperature and chemical composition. Finally, the present work can be seen as a continuation of our detailed crystal chemical study on synthetic clinopyroxene compositions, which now progresses from Li- and Na-rich compositions toward Ca-rich ones (Redhammer et al. 2000; Redhammer and Roth 2002, 2004a, 2004b).

Experimental details

Samples with compositions $(Ca^{2+}_{1-x}Na_x)(Fe^{2+}_{1-x}Fe^{3+}_x)Si_2O_6$ were prepared by a two-step process. In the first step, samples along the solid-solution series (x intervals between 0.05 and 0.1) were synthesized using standard hydrothermal techniques (externally heated, cold-sealed Tuttle-type pressure vessels) at a temperature of 973 K and at a pressure of 0.4 GPa. Oxygen fugacities were controlled by solid-state oxygen buffers [nickel/nickel oxide (NNO) in most cases]. For more details on hydrothermal synthesis of hedenbergite–aegirine clinopyroxenes under controlled oxygen fugacities, the reader is referred to the work of Redhammer et al. (2000). After complete characterization by Mössbauer spectroscopy and powder X-ray diffraction (XRD), these hydrothermally pre-synthesized and fine-grained samples (cf. Fig. 1 in Redhammer et al. 2000) were transferred into small platinum tubes, which, in turn, were placed into a high-pressure Piston-cylinder apparatus (RWTH Aachen). Single-crystal synthesis was done at temperatures ranging from 1473 to 1673 K and pressures ranging from 3.0 to 4.0 GPa. This procedure resulted in dark green-black single crystals up to 100 μm in size. Toward hedenbergite-rich compositions, run batches contained substantial amounts of homogenous gray-green glass. By this two-step method, crystals of 16 different compositions along the solid-solution series were prepared. High-pressure experiments, starting with oxide mixtures, were not successful. Table 1 lists experimental conditions and results of mineral synthesis.

Best-suited single crystals of the high-pressure experiments were fixed onto glass capillaries (0.1 mm diameter) using nail polish. Collection of single-crystal XRD intensity data was done using an imaging-plate diffractometer system (Stoe-IPDS, Mo$K\alpha$ radiation, pyrolytic graphite monochromator). The system was equipped with a cryostream liquid N_2-cryostate (80–300 K, accuracy at least 1 K). All data sets were collected at a crystal to detector distance of 60 mm within a ϕ–range of 0 to 310°; the frame increment was 2°. The absorption correction was done empirically via symmetry equivalents using the SHAPE software (Stoe and Cie 1996). Structure solution (using Patterson methods) and subsequent refinement was carried out with the programs SHELXS-97 and SHELXL-97 (Sheldrick 1997), as implemented in the program suite WinGX 1.64 (Farrugia 1999). X-ray scattering factors in their ionic form, together with anomalous dispersion coefficients, were taken from the *International Tables for Crystallography* (Wilson 1992). All refinements were carried out in space group $C2/c$ with $Z = 4$. An extinction correction was done using the SHELXL method and refinements were carried on until $(\Delta/\sigma) < 0.0001$. During structure refinement, the Fe^{2+}/Fe^{3+} ratio was fixed to the values obtained from ^{57}Fe Mössbauer spectroscopy, as in Redhammer et al. (2000). The chemical compositions of the samples were determined by M2 site refinement in single-crystal structure. It was assumed, that the M1 and the T sites are fully and exclusively occupied by Fe and Si, respectively. Electron microprobe analyses (Redhammer et al. 2000) on hydrothermally synthesized samples on the hedenbergite–aegirine join have shown that this assumption holds true.

Lattice parameters were refined at 298 K from powder XRD data (Siemens D500, Cu$K\alpha$ radiation, secondary graphite monochromator) of ground single crystals, smeared on silicon single-crystal sample holders using Le-Bail whole-pattern refinements as implemented in the program FULLPROF (Rodrigues-Carvajal 2001). Data were collected between 10 and 110° 2θ using silicon (a_o = 5.43094 Å at 298 K) as an internal standard.

Transmission ^{57}Fe Mössbauer spectra between 80 and 700 K were collected using a Mössbauer apparatus in horizontal arrangement (^{57}Co/Rh single line thin source, constant acceleration, symmetric triangular velocity shape, multi-channel analyzer with 1024 channels, velocity calibration to α-Fe). The Mössbauer spectrometer is equipped with an evaporation-cryostate for low-T and with an in-house-designed furnace for high-T measurements. After each cooling and heating experiment series (normally heating-up for high-T and cooling-down for low-T measurements), room-temperature (298 K) Mössbauer spectra of the corresponding sample were recorded to check for any changes in the sample before and after temperature treatment. In no case was there oxidation of samples or changes in relative area proportions, and full reversibility of the changes in Mössbauer spectra as a function of temperature was observed. For Mössbauer absorber preparation, samples were carefully ground under ethanol (to avoid oxidation), mixed with BN_3 (high-temperature investigations) or epoxy resin (low-temperature measurements and 298 K), and filled into Cu rings (inner diameter 10 mm) covered with a high purity Al foil on one side. The folded spectra were analyzed with the Voigt-function-based quadrupole splitting distribution (QSD) method (Rancourt and Ping 1991; Rancourt et al. 1996) implemented in the program suite RECOIL. Using a thin absorber and a single-line thin source, quantum mechanics predicts the absorption (and emission) line in a ^{57}Fe Mössbauer experiment to have Lorentzian line shape. The full width at half maximum Γ thereby is 0.194 mm/s. If broader lines are present, additional physical effects are at work arising from experimental setup and intrinsic characteristics of the sample. These can be modeled by adjusting the width Γ of the Lorentzian components of the spectrum.

A somewhat different approach was used in the Voigt-based QSD method. It was assumed that additional physical features such as thickness effects, dynamic effects, and chemical disorder within solid-solution series cause line broadenings, which are Gaussian in nature. Within the QSD refinement, a certain number m of generalized sites (called QSD-sites from hereon) is used, each having its own continuous quadrupole splitting distribution. Each QSD-site thereby is built up by a certain number of n Gaussian components (Rancourt 1994). The corresponding fitting line-shape is neither Lorentzian nor Gaussian, but is the sum of Voigt lines. For more details on the underlying physics and mathematics of QSD analysis, the reader is referred to the work of Rancourt and coworkers (Rancourt and Ping 1991; Rancourt 1994; Rancourt et al. 1994, 1996 and references therein). In the absence of thickness effects and instrumental broadening, the underlying intrinsic Lorentzian width Γ can be fixed to the natural value (0.194 mm/s). In the present case, Γ was fixed to a value of 0.23 mm/s. This value corresponds to the actual "experimental" line width of the spectrometer in use, and results from calibration spectra on a thin-limit α-Fe foil. Complete thickness correction was applied to all Mössbauer spectra before QSD analysis (Rancourt et al. 1993) as—due to various reasons—different quantities of sample amounts were used for absorber preparation, corresponding to 2.5–15 mg Fe/cm^2. The latter amount is well above the often-invoked value of 5 mg Fe/cm^2 where no effort may be made to estimate the degree of thickness effects (cf. Rancourt et al. 1993). A full thickness correction can easily be done within RECOIL; it is based on the effective Mössbauer thickness, which can be calculated from the chemical composition of the sample as well as its mass and the area of the absorber. From this calculation, the number of ^{57}Fe atoms/cm^2 can be derived. A dimensionless Mössbauer thickness is obtained when multiplied by the intrinsic resonant cross section of the transition. A detailed discussion on Mössbauer absorber thickness is given in Rancourt et al. (1993).

Results

Single-crystal XRD

Examination of systematic extinctions reveals space group $C2/c$ for all compositions investigated here. On pure hedenbergite and sample ac504 with intermediate composition, in-situ low-T measurements were performed to check for changes in symmetry upon cooling between 298 and 100 K. However, both compounds

TABLE 1. Experimental conditions and results of mineral synthesis for clinopyroxenes along the hedenbergite $CaFe^{2+}Si_2O_6$–aegirine $NaFe^{3+}Si_2O_6$ solid-solution series

Sample ID	X(Ae)	Start	*T* (°C)	*P* (GPa)	SSB	d (h)	Product
Hd1	0.00	gel	700	0.4	MW	1006	hd
Hd2	0.00	gel	500	0.4	IQF	240	hd, (qz)
Hd4	0.00	gel	600	0.4	QMF	318	hd, (qz)
Hd5	0.00	gel	600	0.4	IQF	239	hd, (qz)
Hd6	0.00	gel	780	0.18	QMF	308	hd, (qz)
Hd10	0.00	gel	780	0.2	MW	1149	hd
Hd12	0.00	gel	500	0.4	NNO	1269	hd, (qz)
Hd16	0.00	gel	700	0.4	NNO	261	hd, (qz)
Hd20	0.00	gel	650	0.4	MW	1265	hd, (qz)
Hd21	0.00	gel	650	0.4	MW	920	hd, (qz)
Hd22	0.00	gel	700	0.4	MW	689	hd
Hd24	0.00	gel	700	0.4	NNO	689	hd
Hd26	0.00	Hd6	600	0.4	IQF	144	hd, (qz)
Hd21	0.00	Hd6	1300	3.0	–	69	Hd-xx, glas
Ae051	0.05	oxid	700	0.2	NNO	477	cpx
Ae051	0.05	Ae05/1	1300	3.0	–	72	cpx-xx, glas
Ae101	0.10	gel	700	0.4	MW	816	cpx
Ae103	0.10	gel	500	0.4	MW	766	cpx, (qz)
Ae1020	0.10	gel	650	0.4	MW	1006	cpx
Hd102m	0.10	Ae101	1350	3.0	–	67	cpx-xx, glas
Ae151	0.15	oxid	700	0.2	fb	623	cpx, (qz)
Ae151	0.15	Ae151	1350	3.0	–	75	cpx-xx, glas
Ae201	0.20	oxid	700	0.2	fb	623	cpx, (qz)
Ae201	0.20	Ae201	1350	3.0	–	61	cpx, glas
Ae251	0.25	gel	700	0.4	MW	1066	cpx, (qz)
Ae252	0.25	gel	700	0.4	MW	1265	cpx, (qz)
Ae253	0.25	gel	600	0.4	NNO	1058	cpx, (qz)
Ae254	0.25	gel	700	0.4	NNO	991	cpx, (qz)
Ae256	0.25	gel	650	0.4	NNO	1269	cpx, (qz)
Ae2520	0.25	gel	700	0.4	f.b.	1265	cpx, (qz)
Ae2521	0.25	gel	700	0.4	f.b.	1215	cpx, (qz)
Ae251	0.25	Ae251	1350	3.0	–	73	cpx-xx, glas
Ae401	0.40	gel	700	0.4	MW	792	cpx
Ae403	0.40	gel	500	0.4	f.b.	766	cpx, (qz)
Ae404	0.40	gel	780	0.4	f.b.	619	cpx
Ae4020	0.40	gel	700	0.4	MW	912	cpx, (qz)
Ae401	0.40	Ae401	1350	3.0	–	67	cpx-xx
Ae451	0.45	oxid	700	0.4	fb	635	cpx
Ae451	0.45	Ae451	1350	4.0	–	56	cpx-xx
Ae50/1	0.50	gel	700	0.4	MW	1006	cpx, (qz)
Ae50/20	0.50	gel	700	0.4	MW	1265	cpx, (qz)
Ae503	0.50	Ae501	1300	3.0	–	76	cpx-xx
Ae504	0.50	Ae501	1350	3.0	–	61	cpx-xx
Ae551	0.55	oxid	700	0.4	fb	734	cpx, (qz)
Ae551	0.55	Ae501	1400	4.0	–		cpx-xx, (glas)
Ae60/1	0.60	gel	700	0.4	f.b.	816	cpx, (qz)
Ae602	0.60	gel	600	0.4	f.b.	792	cpx, (qz)
Ae603	0.60	gel	500	0.4	f.b.	766	cpx, (qz)
Ae604	0.60	gel	780	0.4	f.b.	619	cpx, (qz)
Ae6020	0.60	gel	700	0.4	f.b.	911	cpx, (qz)
Ae601	0.60	Ae601	1400	4.0	–	74	cpx-xx
Ae701	0.70	oxid	700	0.4	f.b.	734	cpx
Ae701	0.70	Ae701	1400	4.0	–	75	cpx-xx
Ae751	0.75	gel	700	0.4	MW	1006	cpx, (qz)
Ae752	0.75	gel	500		f.b.	1269	cpx, (qz, rie)
Ae754	0.75	gel	780	0.2	f.b.	1269	cpx, (qz)
Ae755	0.75	gel	700	0.4	f.b.	991	cpx, (qz)
Ae7520	0.75	gel	700	0.4	MW	977	cpx, (qz)
Ae7521	0.75	gel	600	0.5	HM	258	cpx, (qz)
Ae751	0.75	Ae751	1400	4.0	–	79	cpx-xx
Ae801	0.80	oxid	700	0.4	NNO	692	cpx
Ae801	0.80	Ae801	1400	4.0	–	65	cpx-xx
Ae851	0.85	oxid	700	0.4	NNO	589	cpx
Ae851	0.85	Ae851	1400	4.0	–	78	cpx-xx
Ae9011	0.90	gel	600	0.4	NNO	407	cpx
Ae9013	0.90	gel	700	0.4	NNO	143	cpx
Ae9020	0.90	gel	700	0.4	HM	150	cpx
Ae901	0.90	Ae9013	1400	4.0	–	69	cpx-xx
Ae951	0.95	oxid	700	0.2	HM	143	cpx
Ae951	0.95	Ae951	1400	4.0	–	61	cpx-xx
Ae1007	1.00	gel	700	0.4	HM	95	Ae, (qz)
Ae1009	1.00	gel	600	0.4	HM	237	Ae (qz)
Ae100/F2f	1.00	gel	950	atm.	air	1152	Ae
Nahp2	1.00	oxid	1200	4.0	–	72	Ae-xx

Notes: Start = starting material for synthesis; SSB = solid state oxygen buffer; IQF = iron quartz/fayalite; MW = magnetite/wuestite; QMF = quartz magnetite/fayalite; NNO = nickel/nickeloxide; f.b. = furnace buffered (between QMF and NNO solid state buffer); Product = phases in synthesis product; hd = hedenbergite; cpx = hedenbergite–aegirine solid solution compounds (xx denotes run products with single crystals larger than 50 μm in size); qz = quartz; rie = riebeckite; Ae = aegirine; glas = glass. Abbreviations in parentheses are below 5% of run product.

retain their *C*2/*c* symmetry. Based on the present observations and those of Redhammer and Roth (2002), we can state that no crystallographic phase transition occurs down to 100 K within the hedenbergite–aegirine solid-solution series. Structure solution using Patterson methods and subsequent structure refinement yield the well-known clinopyroxene structure type. Within the solid-solution series investigated here, both the M1 and the M2 sites are affected by cationic substitution. The Ca^{2+} cation on the M2 site (^{VIII}r = 1.12 Å, Shannon and Prewitt 1969) is successively replaced by the slightly larger Na^+ cation (^{VIII}r = 1.16 Å), whereas on M1, Fe^{2+} (^{VI}r = 0.780 Å) is substituted by the smaller Fe^{3+} cation (^{VI}r = 0.645 Å). Variations within all three basic cell parameters of the clinopyroxene crystal structure are to be expected. Table 2 summarizes structural data and details of structure refinements for the samples investigated at 298 K. Table 3[1] lists the fractional atomic coordinates and equivalent isotropic displacement parameters. Table 4 contains selected interatomic distances, bond angles, and distortion parameters for the samples of the $(Ca,Na)FeSi_2O_6$ solid-solution series.

Anisotropic displacement parameters are available from the crystallographic information file (CIF) and a list of structure factors is deposited within the *American Mineralogist* website. Throughout the solid-solution series, the occupation of Ca^{2+} and Na^+ on M2 was refined. From this information, the amount of aegirine component $X_{aegirine}$ was calculated (see Table 2). The amount of Ca^{2+}, found by M2 site-occupancy refinement, fits nicely with the one found by electron microprobe analysis in Redhammer et al. (2000). Furthermore, the Ca^{2+}/Na^+ ratio is identical to the Fe^{2+}/Fe^{3+} ratio found by 298 K Mössbauer spectroscopy within the experimental uncertainty.

Lattice parameters. Figure 1 displays the variation of lattice parameters determined from powder XRD data of high-pressure/high-temperature samples. The incorporation of aegirine into hedenbergite results in a distinct decrease of the *a* and *b* lattice parameter by 1.9 and 2.6%, respectively, for the whole solid-solution series (Figs. 1a and 1b). The *c* lattice parameter

[1] Deposit item AM-06-023, Table 3, and Figures 9, 11, 12, and 14 that are cited later in the paper. Deposit items are available two ways: For a paper copy contact the Business Office of the Mineralogical Society of America (see inside front cover of recent issue) for price information. For an electronic copy visit the MSA web site at http://www.minsocam.org, go to the American Mineralogist Contents, find the table of contents for the specific volume/issue wanted, and then click on the deposit link there.

(Fig. 1c), however, increases by 0.9% from hedenbergite to aegirine and shows pronounced deviations from a linear trend. This pattern is indicative of a non-ideal mixing behavior deviating from Vegard's Law. The monoclinic angle β increases by 2.5% and the distribution of data points shows a slight S-curvature in going from hedenbergite to aegirine composition (Fig. 1d). The unit-cell volume (Fig. 1e) decreases by 4.8% in going from hedenbergite to aegirine.

The M1 site. Figure 2 displays structural variations within the M1 octahedral site. The individual Fe-O bond lengths decrease with increasing Fe^{3+} content (Fig. 2a) because Fe^{3+} is smaller than Fe^{2+}. The most pronounced shortening is observed for the Fe-O2(c1,d1) bond. The O2(c1,d1) O atoms bridge the M1–octahedral strips with the tetrahedral chain. The smallest change is found for the Fe-O1(a1,b1) bond distance, which connects the central M1 cation with the two O atoms in the equatorial plane of the octahedra and which forms a common edge with the neighboring M2 site. The concentration dependence is slightly non-linear. A decrease of the individual Fe-O interatomic distances also was observed by Redhammer et al. (2000), however, the spread of their powder XRD data did not reveal trends as smooth and significant as those found in this study.

Figure 2b displays the variation of the average Fe-O bond lengths as a function of chemical composition. The data determined from single-crystal structure refinement display a smooth trend without much scatter, which slightly deviates from linearity. For comparison, the <Fe-O> bond lengths from Redhammer et al. (2000) are included. Non-linear behavior is not observ-

TABLE 2. Crystallographic data and details of the single-crystal X-ray diffraction structure refinement for clinopyroxenes of the hedenbergite $CaFe^{3+}Si_2O_6$–aegirine $NaFe^{3+}Si_2O_6$ solid solution series

Sample		Hd21	Hd21	Hd21	Ae051	Hd102m	Ae151	Ae201	Ae251
Temperature (K)		298	200	100	298	298	298	298	298
x $NaFe^{3+}Si_2O_6$ (%)		0	0	0	5.1(6)	9.6(7)	15.0(5)	20.2(9)	25.8(6)
a (Å)		9.8450(9)	9.8395(8)	9.8357(8)	9.8354(7)	9.8248(8)	9.8067(9)	9.7929(7)	9.7938(8)
b (Å)		9.0293(8)	9.0177(8)	9.0078(8)	9.0108(7)	8.9973(7)	8.9852(8)	8.9656(7)	8.9685(7)
c (Å)		5.2450(5)	5.2425(5)	5.2408(5)	5.2560(4)	5.2549(4)	5.2586(5)	5.2696(4)	5.2632(4)
β (°)		104.775(7)	104.724(7)	104.664(6)	105.088(6)	105.013(6)	105.356(6)	105.496(6)	105.520(6)
Volume (Å^3)		450.83	449.89	449.20	449.75	448.58	449.37	446.04	445.44
Dx (Mg m^{-3})		3.655	3.663	3.669	3.601	3.610	3.604	3.631	3.636
μ (mm^{-1})		4.964	4.975	4.975	4.715	4.727	4.719	4.754	4.761
Crystal color		pale yellow	pale yellow	pale yellow	green	green	dark green	dark green	dark green
Crystal size (mm)		0.12 x 0.10	0.12 x 0.10	0.12 x 0.10	0.11x 0.09	0.12 x 0.07	0.11 x 0.08	0.13 x 0.08	0.11 x 0.07
		x 0.06	x 0.06	x 0.06	x 0.07	x 0.06	x 0.06	x 0.07	x 0.06
range of 2θ		3.1–56.2	3.1–64.1	3.1–64.1	3.1–56.4	4.3–65.2	3.1–56.2	3.1–56.1	3.1–56.0
Range of:	*h*	–12–12	–14–14	–14–14	–13–12	–13–14	–12–12	–12–12	–12–12
	k	–11–11	–13–12	–12–12	–11–11	–13–13	–11–11	–11–10	–11–11
	l	–6–6	–7–7	–7–7	–6–6	–7–8	–6–6	–4–6	–6–6
No. Ref.		2427	2646	3311	2185	3044	2152	1175	2080
No. Ref. unique		543	731	759	516	819	535	523	528
R_{int} (%)		2.80	4.06	4.03	2.96	3.84	2.89	2.48	2.72
$R_1 > 4\sigma$ (%)		1.99	1.61	1.55	1.71	2.80	2.14	2.05	1.85
R_1 all data (%)		2.40	1.92	1.80	2.25	5.93	3.17	3.01	3.02
wR_2 all data (%)		5.60	3.75	3.62	6.39	6.28	5.98	5.89	3.56
Goodness of fit		1.175	1.104	1.135	1.051	1.062	0.985	1.012	0.9339
Weighting coeff.		0.0329/0.2718	0.0162/0.1406	0.0154/0.2150	0.0203	0.0283/0.4044	0.0309	0.0308	0.0191
$\Delta\rho_{max}$, $\Delta\rho_{min}$ (eÅ^3)		0.47/–0.40	0.51/–0.38	0.44/–0.35	0.35/–0.45	0.62/–0.65	0.42/–0.43	0.41/–0.51	0.33/–0.31
Extinction coeff.		0.0225(12)	0.0258(7)	0.0222(6)	0.0050(8)	0.0003(7)	0.0019(7)	0.0049(10)	–

Sample		Ae504	Ae504	Ae601	Ae701	Ae751	Ae801	Ae851	Ae901
Temperature (K)		200	90	298	298	298	298	298	298
x $NaFe^{3+}Si_2O_6$ (%)		49.7(4)	49.9(6)	60.4(6)	71.1(8)	75.1(7)	82.5(7)	85.1(7)	89.8(7)
a (Å)		9.7361(8)	9.7266(8)	9.7176(8)	9.6993(8)	9.6953(7)	9.6804(8)	9.6654(8)	9.6666(8)
b (Å)		8.9020(7)	8.8959(7)	8.8792(8)	8.8579(6)	8.8491(7)	8.8337(7)	8.8184(8)	8.8099(7)
c (Å)		5.2733(5)	5.2691(5)	5.2828(6)	5.2813(4)	5.2856(5)	5.2831(6)	5.2805(6)	5.2916(5)
β (°)		106.099(6)	106.067(6)	106.530(6)	106.637(8)	106.778(7)	106.877(7)	106.976(7)	107.195(6)
Volume (Å^3)		439.12	438.11	436.98	434.75	434.17	432.32	430.46	430.50
Dx (Mg m^{-3})		3.624	3.632	3.576	3.595	3.599	3.615	3.631	3.630
μ (mm^{-1})		4.57	4.57	4.315	4.338	4.343	4.361	4.381	4.380
Crystal color		dark green	dark green	dark green	dark green	green	green	green	pale green
Crystal size (mm)		0.09 × 0.08	0.09 × 0.08	0.13 × 0.07	0.11 × 0.07	0.10 × 0.05	0.12 × 0.07	0.13 × 0.08	0.11 × 0.08
		× 0.06	× 0.06	× 0.06	× 0.06	× 0.05	× 0.07	× 0.08	× 0.07
range of 2θ		2.1–56.6	2.1–56.6	3.1–56.0	4.4–55.7	4.61–55.8	4.40–55.7	3.19–56.4	3.20–56.2
Range of:	*h*	–12–12	–12–12	–12–12	–12–12	–12–12	–12–12	–12–12	–12–12
	k	–11–8	–11–8	–11–1	–11–11	–11–11	–11–11	–11–11	–11–11
	l	–6–6	–6–6	–6 –6	–6–6	–6–6	–6–6	–6–6	–6–6
No. Ref.		1565	1579	2320	2087	2076	2072	2069	2045
No. Ref. unique		510	514	525	508	518	514	494	514
R_{int} (%)		2.90	2.72	3.28	9.01	5.05	6.71	3.15	9.70
$R_1 > 4\sigma$ (%)		1.77	1.93	1.84	2.89	2.30	3.27	1.97	2.22
R_1 all data (%)		2.24	2.45	3.07	4.96	4.33	6.90	4.14	3.91
wR_2 all data (%)		4.54	6.70	4.29	5.72	4.60	7.56	4.36	5.17
Goodness of fit		1.421	1.356	0.992	0.856	0.968	1.017	0.974	1.081
weighting coeff.		0.0254	0.0335	0.018/0.7335	0.0176	0.0183	0.0333/0.6628	0.0242	0.0084
$\Delta\rho_{max}$, $\Delta\rho_{min}$ (eÅ^3)		0.41/– 0.37	0.37/–0.38	0.35/–0.36	0.62/–0.78	0.49/–0.37	0.71/–0.92	0.32/–0.39	0.37/–0.63
Extinction coeff.		0.0035(6)	0.0021(7)	–	–	–	0.0078(12)	–	–

able in the latter data. Redhammer et al. (2000) were unable to obtain systematic variations of O-O interatomic distances and of polyhedral distortion parameters, but this was possible in the present study.

The shortening of the Fe-O distances along the hedenbergite–aegirine binary join goes hand in hand with the distinct decrease of the O-O distances (= lengths of the M1 octahedral edges; Fig. 2c). Unshared O-O M1-edges (e_u) show a slightly smaller decrease than the shared O-O M1-edges (e_s) when going from hedenbergite to aegirine. The ratio e_u/e_s, thus, increases from 1.023 in hedenbergite to 1.034 in aegirine. The more pronounced reduction of the shared edges, e_s, may arise from a shielding effect where O atoms approach, avoiding increasing repulsion between Fe^{3+} cations at the M1 site due to the reduction of the M1-O bonds. This behavior also correlates with the off-centering of the M1 cation along the **b**-axis toward M2 and the reduction of the O1a2-Fe-O1b2 angle. The latter can be brought into contact with electrostatic repulsion between neighboring M1 sites as Fe^{3+}-Fe^{3+} pairs become more probable at a local scale with increasing amounts of the aegirine component.

In aegirine, the M1 octahedron displays a distinctly larger deviation from ideal octahedral geometry than the one in hedenbergite (Table 4). This difference is expressed by an increase of the distortion parameters ELD (= edge lengths distortion; Renner and Lehmann 1986), BLD (= bond lengths distortion; Renner and Lehmann 1986), and OAV (= octahedral angle variance; Robinson et al. 1971), the ELD is shown as an example in Figure 2d.

Figure 3 compares the geometry of the M1 octahedron in hedenbergite and aegirine. The most pronounced change in bond angles is observed for the O1-Fe-O1 angle, which is 178.8° in hedenbergite, but decreases by 5.6% to 168.8° in aegirine. In aegirine, the M1 cation has moved out of the center of the M1 octahedron. The O1-M1-O2 bond angle lying in the equatorial plane of the octahedron decreases from 173.0 in hedenbergite to 167.6° in aegirine (decrease by 3.14%).

Although there is a decrease in the individual and mean M1-O bond lengths with increasing aegirine component, the interatomic distance between neighboring M1 cations within the M1 zigzag chain increases by 2.57% from 3.109 Å in hedenbergite to 3.189 Å in aegirine (Fig. 4a). The pronounced increase of the M1-O-M1 angle and—connected with this—the movement of the M1 cation out of the octahedral center and toward the O2 oxygen atom causes the M1 cations to move apart from each other. The non-linear variation of the M1-M1 interatomic distances within the chain along the Hd–Ae series probably is related to the increasing probability to have Fe^{3+} pairs with increasing Ae component. In this regard, it is interesting to note that when comparing the bond-length distortion of the M1 site with the M1-M1 intrachain distance, there are two linear trends that change slope at composition $Hd_{50}Ae_{50}$ (Fig. 4b). The M1-M1 interatomic distance between the M1 zigzag chains decreases with increasing content of the aegirine component (Fig. 4c). In Figures 4a and 4c, data obtained by Redhammer et al. (2000) from Rietveld refinements of powder XRD patterns are included for comparison.

The M2 site. Figure 5 displays the structural variations within the M2 site, induced by the coupled substitution $^{M2}Ca^{2+} + {}^{M1}Fe^{2+} \leftrightarrow {}^{M2}Na^{+} + {}^{M1}Fe^{3+}$. The plot of the individual bond lengths shows that the M2-O1(a1,b1) and the M2-O2(c2,d2) interatomic distances increase slightly by 2.9 and 1.4%, respectively, with increasing aegirine component (Fig. 5a). Pronounced changes are found for the M2-O3 interatomic distances. Here, M2-O3(c1,d1) decreases by 7.3% from hedenbergite to aegirine, whereas the M2-O3(c2,d2) bond length increases by 4.3%. From Figure 5a, it is evident that, toward aegirine-rich compositions, the M2 cation gradually approaches a 6+2-fold coordination, whereas in hedenbergite it exhibits a 4+4-fold coordination. The reason for the drastic changes within the M2 site coordination sphere is due to the substitution of Ca^{2+} by the larger Na^{+} to some extent, but the dominant effect is the different kinking of the neighboring tetrahedral chains. Despite the pronounced changes in the

TABLE 2. —Extended

Ae401	Ae451	Ae503	Ae504
298	298	298	298
38.5(8)	45.0(8)	49.4(5)	51.2(7)
9.7560(7)	9.7428(8)	9.7412(8)	9.7412(8)
8.9252(7)	8.9091(7)	8.9086(7)	8.9086(7)
5.2739(4)	5.2750(5)	5.2776(5)	5.2776(4)
106.031(5)	106.126(5)	106.221(5)	106.221(5)
441.36	439.85	439.76	439.76
3.605	3.682	3.618	3.618
4.539	4.821	4.555	4.555
dark green	dark green	dark green	dark green
0.12 x 0.08	0.13 x 0.11	0.12 x 0.08	0.09 x 0.08
x 0.07	x 0.07	x 0.07	x 0.06
3.1–56.4	3.1–56.4	3.1–56.4	3.1–52.7
–12–12	–12–12	–12–12	–12–11
–11–11	–11–11	–11–11	–11–11
–6–6	–6–6	–6–6	–6–6
2121	2124	2074	1808
533	535	505	441
3.10	7.69	4.41	3.69
1.67	3.26	2.33	2.54
2.81	8.37	5.16	5.23
4.72	5.09	5.58	5.50
1.046	0.888	0.946	1.080
0.0195/0.6349	0.0147	0.0327	0.0170/2.478
0.38/–0.35	0.76/–0.67	0.47/–0.51	0.64/–0.52
0.0015(6)	0.0013(5)	0.0041(8)	0.0002(6)

Ae951	nahp2a
298	298
95.1(4)	100
9.6554(8)	9.6554(7)
8.7998(8)	8.7952(7)
5.2900(6)	5.2942(4)
107.304(5)	107.396(5)
429.12	429.03
3.642	3.577
4.395	4.122
yellow	pale yellow
0.12 × 0.07	0.12 × 0.08
× 0.06	× 0.08
3.20–54.2	3.20–56.2
–12–12	–12–12
–11–11	–11–11
–6–6	–6–6
2078	2497
501	514
3.47	2.72
2.07	2.10
3.07	2.83
5.18	6.79
0.920	1.204
0.0344	0.0413
0.49/–0.48	0.65/–0.51
–	–

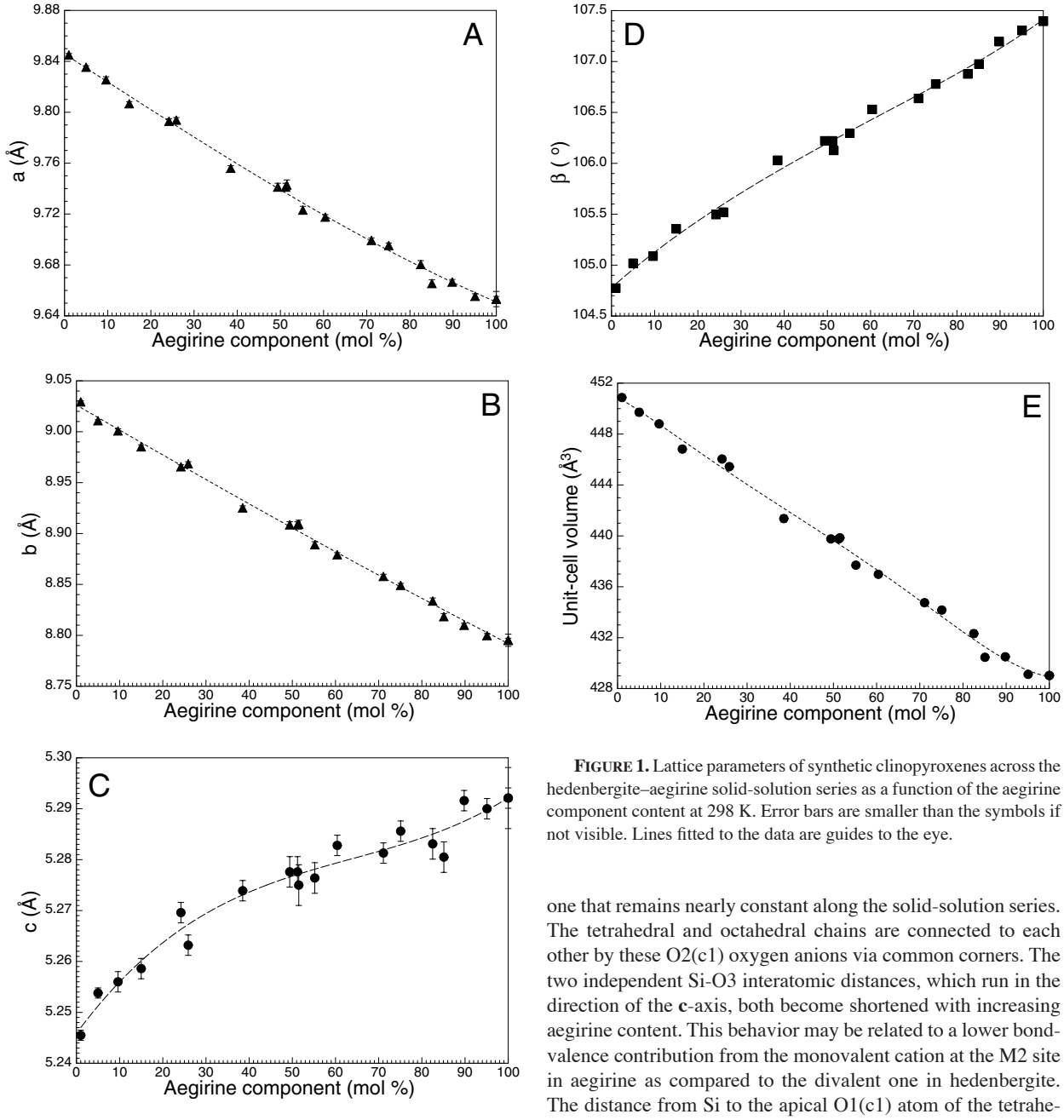

FIGURE 1. Lattice parameters of synthetic clinopyroxenes across the hedenbergite–aegirine solid-solution series as a function of the aegirine component content at 298 K. Error bars are smaller than the symbols if not visible. Lines fitted to the data are guides to the eye.

individual M2-O bond lengths, the average <M2-O> bond length does not change very much (Fig. 5b). There is a slight increase of <M2-O> toward aegirine-rich compositions, which was not observable in the data of Redhammer et al. (2000). In terms of the BLD parameter, the M2 site is as strongly distorted in both hedenbergite and aegirine, whereas at intermediate compositions, the M2 site appears to be less distorted (Fig. 5c). This behavior is induced by the approach of M2-O3(c1,d1) to <M2-O> at intermediate compositions.

The tetrahedral site. Within the tetrahedral chain, some pronounced changes in individual Si-O bond lengths were found (Fig. 6a). The Si-O2(c1) interatomic distance is the only one that remains nearly constant along the solid-solution series. The tetrahedral and octahedral chains are connected to each other by these O2(c1) oxygen anions via common corners. The two independent Si-O3 interatomic distances, which run in the direction of the **c**-axis, both become shortened with increasing aegirine content. This behavior may be related to a lower bond-valence contribution from the monovalent cation at the M2 site in aegirine as compared to the divalent one in hedenbergite. The distance from Si to the apical O1(c1) atom of the tetrahedra becomes slightly larger, which likely is associated with the higher charge contribution from Fe^{3+}. On average, the <Si-O> distance is about 0.01 Å shorter in aegirine than in hedenbergite (Fig. 6b). From the variations of individual Si-O bond lengths, it follows that the average $Si\text{-}O_{br}$ distance decreases whereas the average $Si\text{-}O_{nbr}$ distances increase with increasing the aegirine component (where "br" and "nbr" refer to bridging and non-bridging O atoms, respectively). Consequently, the difference d_{br-nbr} decreases (Fig. 6c). According to Ohashi (2003), decreasing d_{br-nbr} correlates with increasing electronegativity of the M-site cation in clinopyroxenes. This finding holds true here, as Fe^{3+} has a higher electronegativity than Fe^{2+}. The bond-length distortion of individual Si-O bonds decreases from 2.5% in hedenbergite to

TABLE 4. Selected bond lengths (Å), bond angles (°), and distortion parameters of selected synthetic clinopyroxenes for the hedenbergite $CaFe^{3+}Si_2O_6$–aegirine $NaFe^{3+}Si_2O_6$ solid-solution series

Sample	Hd21	Hd21	Hd21	Ae051	Hd102m	Ae151	Ae201	Ae251	Ae401	Ae451	Ae503	Ae504
Temperature (K)	298	200	100	298	298	298	298	298	298	298	298	298
M2-O2c2,d2 (Å)	2.339(1)	2.338(1)	2.336(1)	2.341(2)	2.349(2)	2.364(2)	2.362(2)	2.363(2)	2.367(2)	2.386(3)	2.378(2)	2.375(3)
M2-O1a1,b1 (Å)	2.358(1)	2.353(1)	2.353(1)	2.361(1)	2.364(2)	2.381(2)	2.376(2)	2.378(2)	2.380(2)	2.390(4)	2.390(2)	2.391(3)
M2-O3c1,d1 (Å)	2.628(1)	2.626(1)	2.627(1)	2.613(1)	2.601(2)	2.580(2)	2.568(2)	2.566(2)	2.540(2)	2.515(4)	2.518(2)	2.519(3)
M2-O3c2,d2 (Å)	2.720(1)	2.709(1)	2.698(1)	2.732(1)	2.731(2)	2.739(2)	2.747(2)	2.748(2)	2.761(2)	2.776(4)	2.777(2)	2.772(3)
<M2-O> (Å)	2.511	2.506	2.504	2.512	2.511	2.516	2.513	2.514	2.512	2.517	2.516	2.514
BLD (%)	6.48	6.43	6.35	6.40	6.16	5.70	5.74	5.70	5.51	5.15	5.24	5.22
Fe-O2c1,d1 (Å)	2.087(1)	2.087(1)	2.085(1)	2.077(1)	2.070(2)	2.055(2)	2.044(2)	2.046(2)	2.024(2)	2.012(3)	2.010(2)	2.013(3)
Fe-O1a2,b2 (Å)	2.138(1)	2.140(1)	2.138(1)	2.125(2)	2.125(2)	2.116(2)	2.105(2)	2.102(2)	2.086(2)	2.075(3)	2.077(2)	2.075(3)
Fe-O1a1,b1 (Å)	2.162(1)	2.159(1)	2.157(1)	2.160(1)	2.156(2)	2.152(2)	2.143(2)	2.144(2)	2.132(2)	2.129(3)	2.128(2)	2.132(3)
<M1-O> (Å)	2.129	2.129	2.127	2.121	2.117	2.108	2.097	2.097	2.081	2.072	2.072	2.073
BLD (%)	1.32	1.31	1.31	1.37	1.48	1.67	1.70	1.63	1.82	1.93	1.98	1.94
ELD (%)	2.45	2.45	2.424	2.43	2.46	2.55	2.65	2.68	2.77	2.95	2.86	2.86
OAV (°)	16.3	16.4	15.9	17.2	17.9	20.6	22.7	22.9	27.4	32.1	32.5	32.3
<O-O> (Å)	3.009	3.009	3.006	2.997	2.993	2.978	2.963	2.963	2.939	2.926	2.925	2.928
$<O\text{-}O>_s = e_s$ (Å)	2.970	2.967	2.966	2.952	2.950	2.927	2.911	2.913	2.883	2.875	2.871	2.873
$<O\text{-}O>_u = e_u$ (Å)	3.038	3.039	3.035	3.030	3.023	3.014	3.000	2.999	2.979	2.963	2.964	2.967
e_u/e_s	1.023	1.024	1.023	1.027	1.025	1.030	1.031	1.029	1.033	1.031	1.032	1.033
Fe-Fe (intra) (Å)	3.109(1)	3.103(1)	3.098(1)	3.118(1)	3.121(1)	3.142(1)	3.139(1)	3.137(1)	3.148(1)	3.156(1)	3.159(1)	3.160(1)
Fe-Fe (inter) (Å)	5.711(1)	5.712(1)	5.714(1)	5.687(1)	5.681(1)	5.655(1)	5.635(1)	5.632(1)	5.583(1)	5.564(1)	5.558(1)	5.557(1)
Si-O2 (Å)	1.589(1)	1.587(1)	1.587(1)	1.591(1)	1.589(2)	1.596(2)	1.595(2)	1.593(2)	1.591(2)	1.585(3)	1.593(2)	1.594(3)
Si-O1 (Å)	1.601(1)	1.603(1)	1.602(1)	1.605(1)	1.603(2)	1.609(2)	1.613(2)	1.612(2)	1.614(2)	1.615(3)	1.615(2)	1.614(3)
Si-O3 (Å)	1.668(1)	1.669(1)	1.670(1)	1.666(1)	1.666(2)	1.672(2)	1.661(2)	1.659(2)	1.657(2)	1.654(4)	1.652(2)	1.656(3)
Si-O3 (Å)	1.684(1)	1.687(1)	1.686(1)	1.685(1)	1.683(2)	1.686(2)	1.683(2)	1.679(2)	1.673(2)	1.668(3)	1.670(2)	1.662(3)
<Si-O> (Å)	1.636	1.636	1.636	1.637	1.635	1.641	1.638	1.636	1.634	1.631	1.633	1.632
$d_{br\text{-}nbr}$ (Å)	0.081	0.083	0.083	0.078	0.079	0.077	0.068	0.067	0.063	0.061	0.057	0.055
BLD (%)	2.48	2.53	2.55	2.37	2.40	2.33	2.08	2.03	1.91	1.87	1.75	1.67
TAV (°)	25.0	25.1	25.4	23.9	24.4	23.3	22.6	21.7	20.1	20.0	19.3	18.4
Tau (°)	112.7(1)	112.7(1)	112.8(1)	112.6(1)	112.6(1)	112.3(1)	112.3()	112.2(1)	112.0(1)	111.8(1)	111.8(1)	111.8(1)
Si-O3-Si	136.0(1)	135.8(1)	135.7(1)	136.3(1)	136.3(1)	136.7(1)	136.8(1)	136.9(1)	137.3(1)	137.9(1)	137.7(1)	137.6(1)
O3-O3-O3 (°)	164.5(1)	164.2(1)	163.9(1)	165.2(1)	165.7(1)	166.7(1)	167.0(1)	167.2(1)	168.1(1)	169.8(1)	169.4(1)	169.4(1)

Sample	Ae504	Ae504	Ae601	Ae701	Ae751	Ae801	Ae851	Ae901	Ae951	nahp2a
Temperature (K)	200	100	298	298	298	298	298	298	298	298
M2-O2c2,d2 (Å)	2.377(1)	2.374(1)	2.390(2)	2.394(4)	2.399(2)	2.402(4)	2.403(2)	2.414(2)	2.406(2)	2.406(2)
M2-O1a1,b1 (Å)	2.387(1)	2.383(1)	2.398(2)	2.390(4)	2.397(2)	2.401(4)	2.396(2)	2.403(2)	2.395(2)	2.392(2)
M2-O3c1,d1 (Å)	2.521(1)	2.520(1)	2.495(2)	2.481(4)	2.481(2)	2.463(4)	2.455(2)	2.442(2)	2.441(2)	2.436(2)
M2-O3c2,d2 (Å)	2.767(1)	2.759(1)	2.783(2)	2.793(4)	2.794(2)	2.798(4)	2.805(2)	2.815(2)	2.824(2)	2.838(2)
<M2-O> (Å)	2.513	2.509	2.517	2.515	2.518	2.516	2.515	2.519	2.517	2.518
BLD (%)	5.21	5.20	5.30	5.54	5.49	5.60	5.77	5.89	6.11	6.35
Fe-O2c1,d1 (Å)	2.007(1)	2.006(1)	1.988(2)	1.983(4)	1.966(2)	1.957(3)	1.951(2)	1.943(2)	1.940(2)	1.934(2)
Fe-O1a2,b2 (Å)	2.076(1)	2.075(1)	2.061(2)	2.054(3)	2.047(2)	2.042(3)	2.039(2)	2.037(2)	2.031(2)	2.030(2)
Fe-O1a1,b1 (Å)	2.124(1)	2.122(1)	2.121(2)	2.122(4)	2.117(2)	2.119(3)	2.112(2)	2.112(2)	2.110(2)	2.112(2)
<M1-O> (Å)	2.069	2.068	2.057	2.053	2.043	2.039	2.034	2.031	2.027	2.025
BLD (%)	1.99	1.99	2.23	2.27	2.52	2.69	2.72	2.88	2.86	3.01
ELD (%)	2.87	2.85	3.01	3.08	3.12	3.13	3.18	3.21	3.01	3.20
OAV (°)	32.4	31.3	38.8	40.9	45.4	47.2	50.4	54.0	55.0	56.0
<O-O> (Å)	2.921	2.920	2.903	2.897	2.884	2.879	2.870	2.865	2.864	2.857
$<O\text{-}O>_s = e_s$ (Å)	2.865	2.863	2.848	2.839	2.828	2.827	2.816	2.813	2.804	2.802
$<O\text{-}O>_u = e_u$ (Å)	2.961	2.961	2.943	2.939	2.924	2.915	2.908	2.901	2.907	2.896
e_u/e_s	1.033	1.034	1.033	1.035	1.034	1.031	1.032	1.031	1.037	1.034
Fe-Fe (intra) (Å)	3.154(1)	3.148(1)	3.167(1)	3.168(2)	3.174(1)	3.178(2)	3.178(1)	3.185(1)	3.185(1)	3.189(1)
Fe-Fe (inter) (Å)	5.561(1)	5.561(1)	5.526(1)	5.508(2)	5.495(1)	5.483(2)	5.464(1)	5.452(1)	5.441(1)	5.431(1)
Si-O2 (Å)	1.597(1)	1.597(1)	1.596(2)	1.591(4)	1.598(2)	1.595(3)	1.595(2)	1.600(2)	1.596(2)	1.600(2)
Si-O1 (Å)	1.619(1)	1.619(1)	1.621(2)	1.621(4)	1.626(2)	1.624(3)	1.623(2)	1.624(2)	1.626(2)	1.627(2)
Si-O3 (Å)	1.650(1)	1.651(1)	1.649(2)	1.641(4)	1.638(2)	1.639(3)	1.641(2)	1.643(2)	1.638(2)	1.634(2)
Si-O3 (Å)	1.671(1)	1.668(1)	1.665(2)	1.664(4)	1.666(2)	1.657(3)	1.650(2)	1.645(2)	1.649(2)	1.648(2)
<Si-O> (Å)	1.634	1.634	1.633	1.629	1.632	1.629	1.627	1.628	1.627	1.627
$d_{br\text{-}nbr}$ (Å)	0.052	0.052	0.049	0.047	0.040	0.039	0.037	0.032	0.033	0.028
BLD (%)	1.59	1.59	1.49	1.43	1.23	1.18	1.12	0.98	1.00	0.85
TAV (°)	18.9	18.5	17.79	16.02	16.27	16.47	15.50	14.33	14.54	14.70
Tau (°)	111.8(1)	111.8(1)	111.6(1)	111.5(1)	111.4(1)	111.7(1)	111.3(1)	111.2(1)	111.1(1)	111.1(1)
Si-O3-Si	137.6(1)	137.5(1)	138.1(1)	138.3(1)	138.5(1)	138.7(1)	138.7(1)	139.0(1)	139.1(1)	139.3(1)
O3-O3-O3	168.9(1)	168.7(1)	170.3(1)	170.9(1)	170.8(1)	172.0(1)	172.4(1)	173.4(1)	173.3(1)	173.8(1)

Notes: {Equation 1 below} %, n= amount of cation-anion bonds and X-O = cation-anion (oxygen) distance (Renner and Lehmann 1986); *{Equation 2 below}* %, n = amount of edges and (O-O) = oxygen-oxygen interatomic distance defining an edge of the octahedron (Renner and Lehmann 1986); *{Equation 3 below}* with Θ_i = O-M-O bonding angle (Robinson et al. 1971); *{Equation 4 below}* with Θ_i = O-T-O bonding angle (Robinson et al. 1971); e_u/e_s = ratio between unshared (e_u) and shared (e_s) octahedral edges (Toraya 1981).

Eq. 1 = $BLD = \frac{100}{n}\sum_{i=1}^{n}\frac{\left|\left(X-O\right)_i - \left(<X-O>\right)\right|}{\left(<X-O>\right)}$ Eq. 2 = $ELD = \frac{100}{n}\sum_{i=1}^{n}\frac{\left|\left(O-O\right)_i - \left(<O-O>\right)\right|}{\left(<O-O>\right)}$ Eq. 3 = $OAV = \sum_{i=1}^{12}\left(\Theta_i - 90^\circ\right)^2 / 11$ Eq. 4 = $TAV = \sum_{i=1}^{6}\left(\Theta_i - 109.57^\circ\right)^2 / 5$

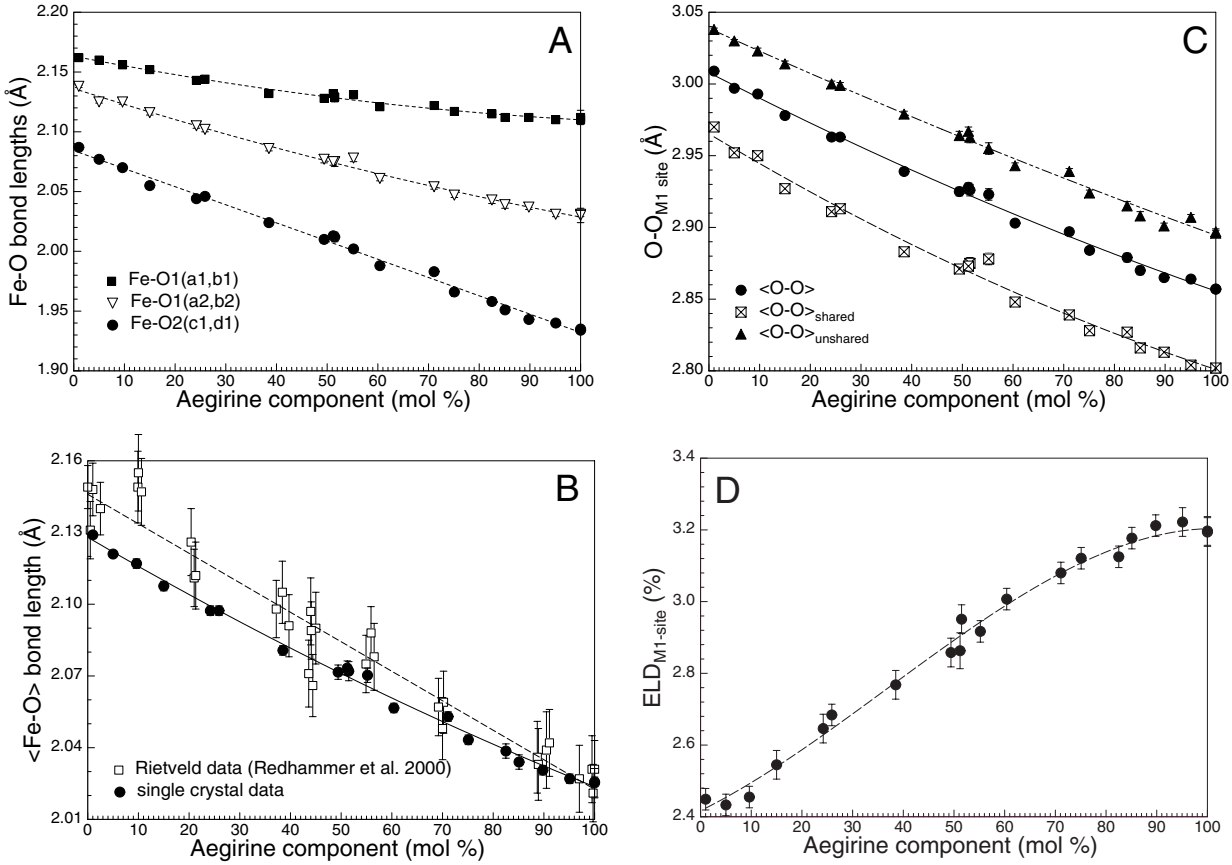

FIGURE 2. Structural parameters of the M1 site of synthetic clinopyroxenes across the hedenbergite–aegirine solid-solution series as a function of the aegirine component content at 298 K: (**a**) individual M1-O bond lengths; (**b**) average M1-O bond lengths in comparison with data of Redhammer et al. (2000); (**c**) oxygen-oxygen atom distances (O-O = edge length of the M1 octahedron); and (**d**) deviation of individual O-O edge lengths from their averaged value = edge-lengths distortion (ELD). Error bars are smaller than the symbols if not visible. Lines fitted to the data are guides to the eye.

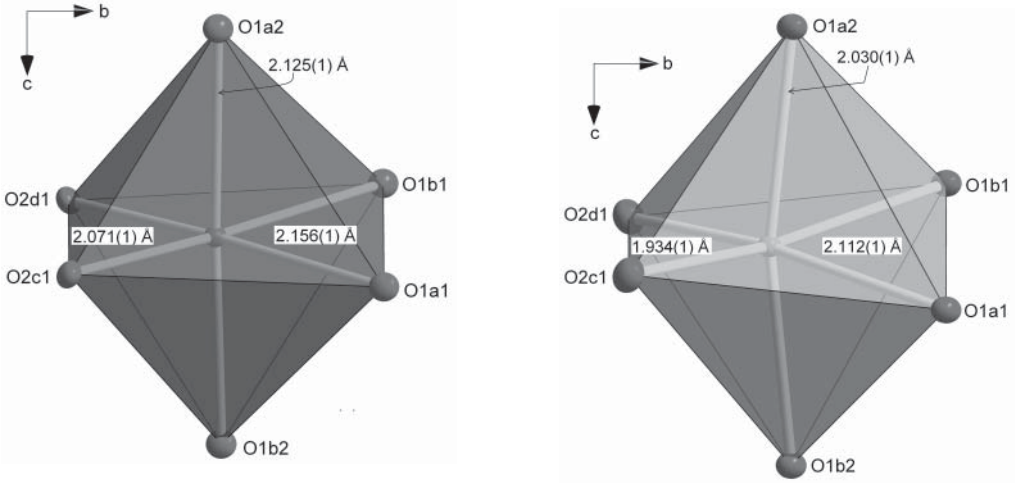

FIGURE 3. Representation of the M1 octahedral geometry viewed along the *a*-axis at 298 K for (**a**) hedenbergite-$CaFe^{2+}Si_2O_6$, and (**b**) aegirine-$NaFe^{3+}Si_2O_6$.

0.85% in aegirine, as does the tetrahedral angle variance (TAV, Table 4). Thus, the geometry of the tetrahedra in aegirine is closer to ideal as compared to the ones in hedenbergite. The angle τ (which is the average of the two O3-Si-O2 and the O1-Si-O2 angles and which defines the elongation state of the tetrahedron) becomes smaller toward aegirine, showing the tetrahedra to

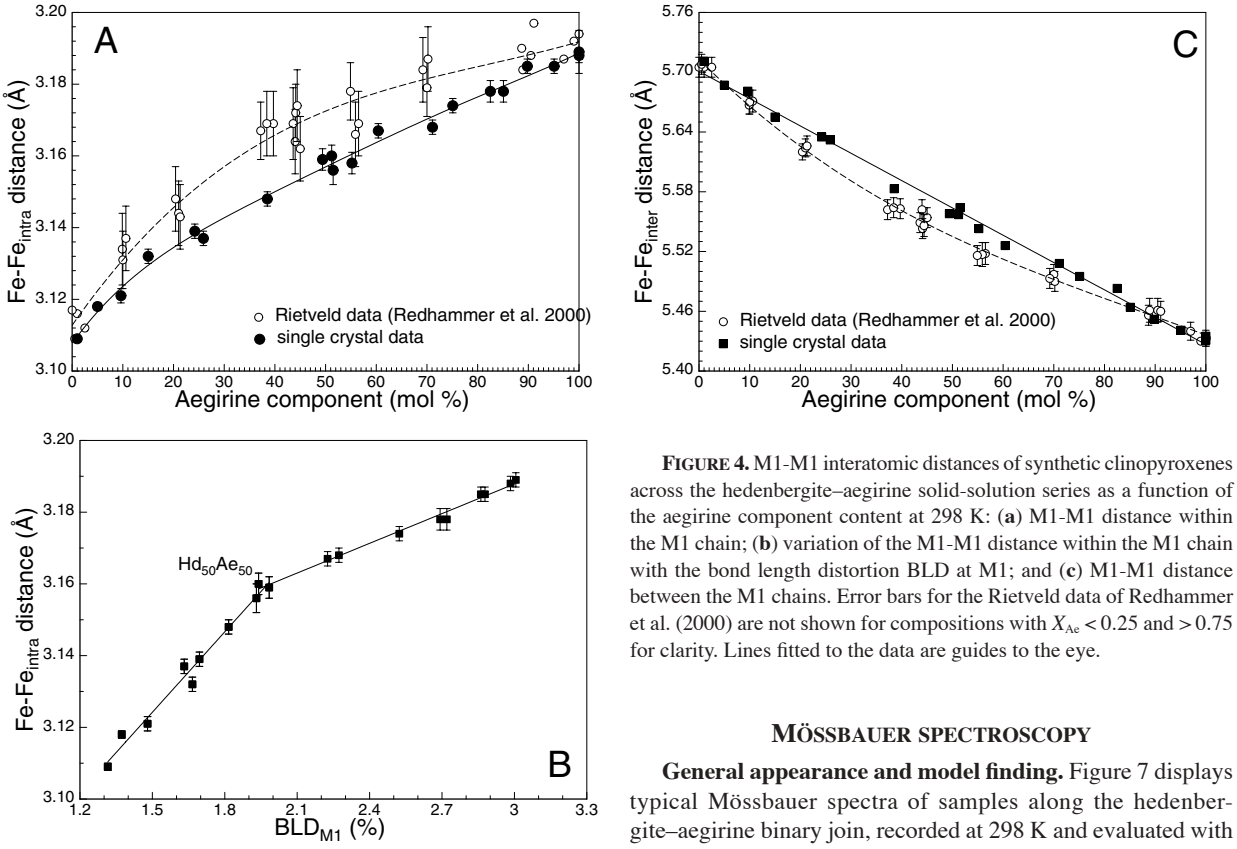

FIGURE 4. M1-M1 interatomic distances of synthetic clinopyroxenes across the hedenbergite–aegirine solid-solution series as a function of the aegirine component content at 298 K: (**a**) M1-M1 distance within the M1 chain; (**b**) variation of the M1-M1 distance within the M1 chain with the bond length distortion BLD at M1; and (**c**) M1-M1 distance between the M1 chains. Error bars for the Rietveld data of Redhammer et al. (2000) are not shown for compositions with $X_{Ae} < 0.25$ and > 0.75 for clarity. Lines fitted to the data are guides to the eye.

be less elongated in aegirine. This behavior goes along with a smooth linear increase in the Si-O3-Si angle from 136.0(1)° in hedenbergite to 139.1(1)° in aegirine (Table 4). The most pronounced change within the tetrahedral chain is the increase of the tetrahedral kinking angle with increasing aegirine content (Fig. 6d). According to this finding, the tetrahedral chain is more kinked in hedenbergite and is straightened by about 10° toward pure aegirine. The chains show an "O" (opposite) rotational sense (Thompson 1970; Papike et al. 1973; Cameron and Papike 1981). Redhammer et al. (2000) found similar trends, although the scatter in their data points was too large to deduce significant non-linear behavior, as shown here in Figure 6d.

Low-temperature measurements on $CaFeSi_2O_6$ and $Ca_{0.5}Na_{0.5}FeSi_2O_6$. Upon cooling from room temperature to 100 K, the unit-cell volume of hedenbergite decreases by 0.36%, a value similar to the one for the intermediate compound and for Na- and Li-clinopyroxenes (Redhammer and Roth 2002, 2004b). Among the bond lengths, <M2-O> is most sensitive for temperature-dependent changes, whereas Si-O bonds are least sensitive. It is well established that large polyhedra, such as the M2 site in clinopyroxene, show a large temperature dependence of bond lengths and angles. However, tetrahedra with strong T-O bonds show only minor changes with temperature (or pressure), except for the SiO_4 polyhedral distortional parameters, which become smaller (i.e., polyhedra become more regular) with decreasing temperature (Table 4). These generalizations hold true for both compounds investigated here at low temperatures.

MÖSSBAUER SPECTROSCOPY

General appearance and model finding. Figure 7 displays typical Mössbauer spectra of samples along the hedenbergite–aegirine binary join, recorded at 298 K and evaluated with the quadrupole splitting distribution approach. ^{57}Fe Mössbauer parameters are compiled in Table 5.

The Mössbauer spectrum of pure synthetic hedenbergite $CaFe^{2+}Si_2O_6$ (Fig. 7a) shows two symmetric and narrow resonance absorption lines contributing to one quadrupole doublet and a low intensity doublet arising from a small Fe^{3+} content. ^{57}Fe hyperfine parameters are typical for high-spin Fe^{2+} in octahedral coordination (isomer shift δ = ~1.19 mm/s, quadrupole splitting ΔE_Q = ~2.26 mm/s; Table 5). Using the QSD method, the spectrum of pure synthetic hedenbergite can be refined perfectly with one QSD site for Fe^{2+} on M1 having a single Gaussian component. The Gaussian width, σ, of this component is 0.00(1)–0.03(1) mm/s, indicating vanishing distribution effects of Fe^{2+} quadrupole splitting in hedenbergite. No hint of Fe^{2+} on the M2 site is present. It should be noted that synthetic hedenbergite could contain significant amounts of Fe^{3+} (up to 5% of total Fe) on the octahedral M1 site when synthesized under oxidizing conditions. Detailed comments and discussion of Fe^{3+} contents and the range of ^{57}Fe hyperfine parameters for Fe^{3+} in hedenbergite can be found in Redhammer et al. (2000).

The Mössbauer spectrum of pure synthetic aegirine also consists of two narrow and symmetric resonance absorption lines contributing to one quadrupole doublet (Redhammer et al. 2000). ^{57}Fe hyperfine parameters are typical for high-spin Fe^{3+} (isomer shift δ = 0.39 mm/s, quadrupole splitting ΔE_Q = 0.29 mm/s). As for hedenbergite, the resonance absorption contribution can be refined perfectly by a model with one QSD-site for Fe^{3+} on M1 having a single Gaussian component. The Gaussian width σ of this component is below σ = 0.03 mm/s (practically

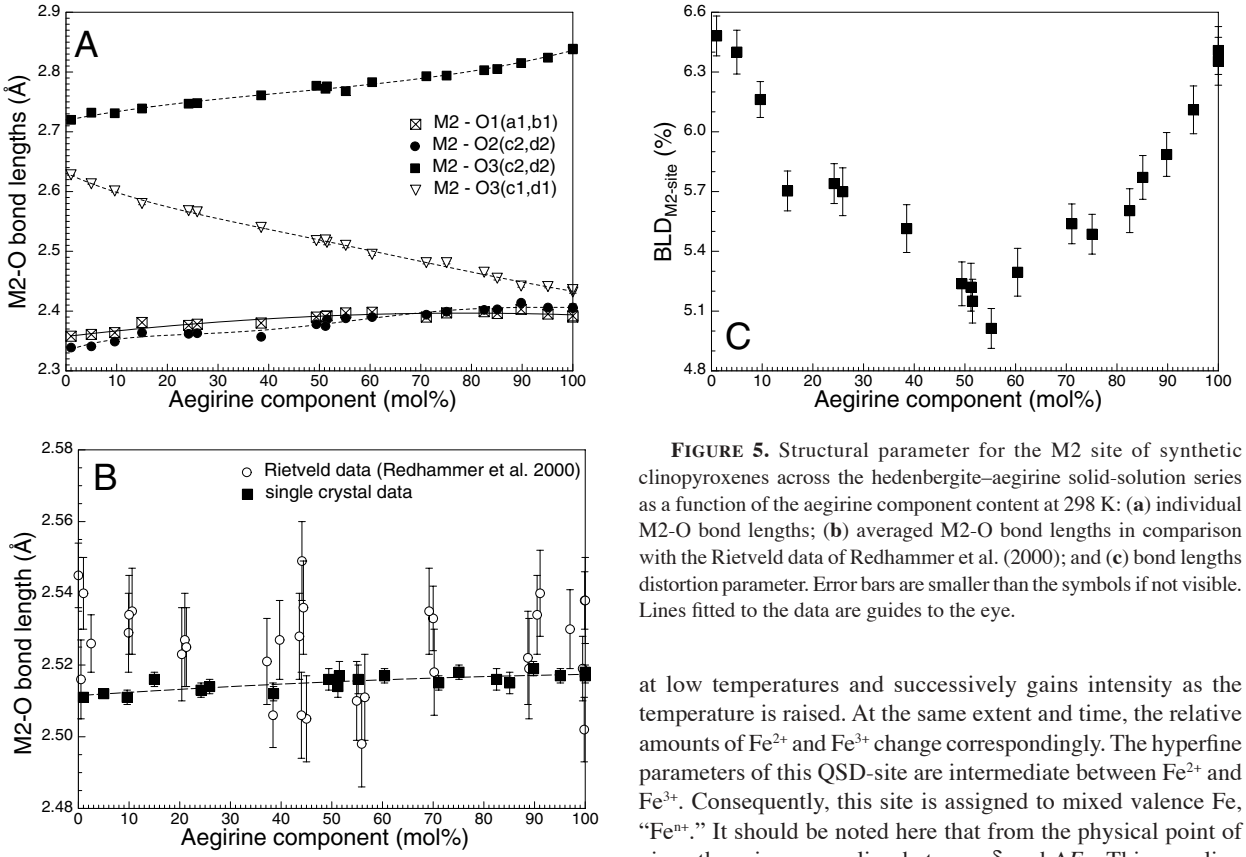

FIGURE 5. Structural parameter for the M2 site of synthetic clinopyroxenes across the hedenbergite–aegirine solid-solution series as a function of the aegirine component content at 298 K: (**a**) individual M2-O bond lengths; (**b**) averaged M2-O bond lengths in comparison with the Rietveld data of Redhammer et al. (2000); and (**c**) bond lengths distortion parameter. Error bars are smaller than the symbols if not visible. Lines fitted to the data are guides to the eye.

no distribution effects).

Due to the replacement of Ca^{2+} by Na^{+}, both Fe^{2+} and Fe^{3+} are present on the M1 site within the hedenbergite–aegirine solid-solution series. As a crystallographic phase transition has not been observed within the solid-solution series, it could be expected that the spectra of the hedenbergite–aegirine mixed crystals are simple mixtures of the two end-member spectra. The situation, however, is more complicated: the Fe^{2+} resonant absorption contribution becomes broadened asymmetrically as the Fe^{3+} component increases (Figs. 7b–7e). It is necessary to use up to three discrete Lorentzian doublets to model the Fe^{2+} resonant absorption contribution to obtain acceptable fits (Dollase and Gustafson 1982; Redhammer et al. 2000). By applying the QSD approach, it was possible to adequately refine the Mössbauer spectra of the mixed crystals by a model with one generalized QSD-site for Fe^{2+} (M1), containing two Gaussian sub-components, and one QSD-site for Fe^{3+} with one Gaussian sub-component. By applying this model, some residual resonance absorption contribution still is present at Doppler velocities between 1.0 and 1.2 mm/s in the 298 K spectra. To take this contribution into account, an additional generalized QSD-site was added. It has two Gaussian sub-components that are allowed to have a distinct coupling between isomer shift δ and quadrupole splitting ΔE_Q according to the formula $\delta = \delta_0 + \delta_1 \cdot \Delta E_Q$ (with δ_1 being the coupling parameter). Due to this coupling, the fitted component appears to be distinctly asymmetric (Figs. 7b–7e); the fitted average hyperfine parameters of this site are reported in Table 5. This QSD-site is not present at low temperatures and successively gains intensity as the temperature is raised. At the same extent and time, the relative amounts of Fe^{2+} and Fe^{3+} change correspondingly. The hyperfine parameters of this QSD-site are intermediate between Fe^{2+} and Fe^{3+}. Consequently, this site is assigned to mixed valence Fe, "Fe^{n+}." It should be noted here that from the physical point of view, there is no coupling between δ and ΔE_Q. This coupling solely is a fitting technique to reproduce the asymmetric nature of the resonance absorption contribution of the "Fe^{n+}" QSD-site. By the linear coupling between δ and ΔE_Q a distribution $P(\Delta E_Q)$ of quadrupole spitting values is obtained that automatically has an associated distribution of isomer shift values (Rancourt et al. 1994).

An Fe^{2+} QSD model with three sub-components also was tried, by analogy with the work of Dollase and Gustafson (1982). Such a three-Fe^{2+}-component model would explain the Fe^{2+} line broadening by discrete M2 NNN configurations. However, refinements with such a model were unstable or did not converge well. The Gaussian width of the additional third Fe^{2+} component was always very close to zero ($\sigma < 0.02$ mm/s) and the relative proportion of Fe^{2+} on this third site also is low (<5% Fe^{2+}). The resulting Fe^{2+} QSD curves were similar to the 2-1-2 model. Moreover, it was impossible to determine the relative proportions of Fe^{2+}, which are the same at room temperature and, e.g., at 80 K, except by applying massive constrains and parameter fixings. Such constrained refinements were statistically worse compared to the completely unconstrained refinements of the 2-1-2 model. Based on these observations, the model with three sub-components for Fe^{2+} was ruled out.

Variation of hyperfine parameters at 298 K. Throughout the entire solid-solution series, the Fe^{3+} site is built up by a single Gaussian component with a small Gaussian width σ (Table 5). The Gaussian broadening of Fe^{3+} slightly decreases with increasing Fe^{3+} content. A similar broadening was observed by Dollase and Gustafson (1982). The isomer shift (Fig. 8a) as well

TABLE 5. ^{57}Fe hyperfine parameters for synthetic clinopyroxenes for the hedenbergite $CaFe^{2+}Si_2O_6$–aegirine $NaFe^{3+}Si_2O_6$ solid solution-series at 298 K

	Fe^{3+}				Fe^{2+}							Fe^{n+}		
Sample	IS	QS	sigma	A	IS	QS-L	sigma	A*	QS-S	sigma	A*	<IS>	<QS>	A
Hd L16a	0.370(13)	1.117(25)	0.09(1)	5.2(5)	1.188(5)	–	–	–	2.239(5)	0.02(1)	100	–	–	–
Hd 1	–	–	–	–	1.193(4)	–	–	–	2.263(4)	0.03(1)	100	–	–	–
Hd 2	0.357(19)	1.004(27)	0.12(1)	3.0(4)	1.193(4)	–	–	–	2.262(4)	0.01(1)	100	–	–	–
Hd 4	0.367(17)	0.999(21)	0.04(3)	3.0(6)	1.194(4)	–	–	–	2.255(3)	0.02(1)	100	–	–	–
Hd 5	–	–	–	–	1.192(3)	–	–	–	2.261(5)	0.02(1)	100	–	–	–
Hd 6	0.354(15)	1.123(18)	0.01(3)	3.3(3)	1.203(5)	–	–	–	2.263(5)	0.01(2)	100	–	–	–
Hd 6/300	0.384(25)	1.084(23)	0.11(2)	3.0(3)	1.194(5)	–	–	–	2.253(4)	0.02(1)	100	–	–	–
Hd 6/400	0.364(17)	1.046(24)	0.10(2)	2.9(4)	1.194(7)	–	–	–	2.252(4)	0.03(2)	100	–	–	–
Hd 12	0.348(23)	1.012(23)	0.07(1)	3.9(5)	1.192(7)	–	–	–	2.254(5)	0.02(1)	100	–	–	–
Hd 16/400	0.374(23)	1.092(22)	0.21(3)	5.3(5)	1.195(4)	–	–	–	2.253(3)	0.03(1)	100	–	–	–
Hd 20	0.352(14)	1.076(14)	0.05(1)	2.6(3)	1.193(4)	–	–	–	2.252(4)	0.03(1)	100	–	–	–
Hd 21	–	–	–	–	1.194(4)	–	–	–	2.263(3)	0.05(2)	100	–	–	–
Hd 22	–	–	–	–	1.193(5)	–	–	–	2.259(3)	0.02(1)	100	–	–	–
Hd 24	0.361(14)	1.092(11)	0.10(2)	2.4(7)	1.196(5)	–	–	–	2.248(4)	0.04(2)	100	–	–	–
Hd 26	–	–	–	–	1.194(4)				2.258(3)	0.02(1)	100	–	–	–
Ae05 1	0.367(14)	1.147(14)	0.14(1)	5.4(6)	1.194(6)	2.633(14)	0.14(1)	9.6(2.1)	2.210(13)	0.10(1)	90.4(1.9)	–	–	–
Ae10 1	0.386(8)	0.746(16)	0.12(1)	11.2(6)	1.177(5)	2.667(21)	0.10(1)	4.7(6)	2.165(9)	0.10(1)	95.3(7)	–	–	–
Ae10 3	0.395(8)	0.697(13)	0.12(1)	11.4(6)	1.178(9)	2.680(22)	0.10(1)	5.0(6)	2.178(6)	0.10(1)	95.0(9)	–	–	–
Ae10 20	0.389(9)	0.725(9)	0.13(2)	11.2(7)	1.189(7)	2.694(23)	0.10(1)	4.6(8)	2.181(10)	0.09(1)	95.4(9)	–	–	–
Ae15 1	0.400(9)	0.542(18)	0.11(3)	15.0(9)	1.203(8)	2.679(15)	0.11(1)	11.9(8)	2.136(11)	0.11(1)	88.1(11)	–	–	–
Ae20 1	0.404(8)	0.506(12)	0.10(1)	20.1(11)	1.202(4)	2.695(12)	0.12(1)	11.4(21)	2.129(7)	0.14(1)	88.6(18)	–	–	–
Ae25 1	0.418(10)	0.476(15)	0.10(2)	19.8(7)	1.193(4)	2.734(11)	0.09(1)	15.4(7)	2.113(5)	0.21(1)	84.6(7)	0.505(9)	1.450(15)	5.4(9)
Ae25 2	0.430(4)	0.466(9)	0.09(1)	18.8(4)	1.208(3)	2.711(9)	0.08(1)	13.5(11)	2.136(6)	0.10(2)	86.5(12)	0.582(8)	1.658(12)	5.4(11)
Ae25 3	0.416(2)	0.468(5)	0.07(1)	19.8(3)	1.182(6)	2.728(13)	0.09(1)	13.9(8)	2.140(4)	0.21(1)	86.1(8)	0.510(8)	1.549(8)	4.6(8)
Ae25 4	0.425(3)	0.469(6)	0.04(3)	20.9(3)	1.192(3)	2.704(16)	0.08(1)	16.9(9)	2.110(4)	0.16(1)	83.1(8)	0.566(7)	1.530(9)	4.7(8)
Ae25 6	0.412(2)	0.463(12)	0.11(3)	20.6(8)	1.183(5)	2.703(11)	0.09(1)	15.8(15)	2.124(7)	0.20(3)	84.2(16)	0.529(9)	1.644(11)	6.1(7)
Ae25 21	0.427(2)	0.464(5)	0.10(1)	20.9(3)	1.185(3)	2.717(8)	0.08(1)	15.4(6)	2.136(4)	0.18(1)	84.7(7)	0.570(9)	1.599(11)	5.4(12)
Ae40 1	0.415(4)	0.431(3)	0.10(1)	35.2(8)	1.184(4)	2.775(13)	0.11(1)	19.1(13)	2.064(9)	0.29(1)	80.9(8)	0.479(8)	1.404(9)	8.0(9)
Ae40 3	0.418(3)	0.440(3)	0.12(1)	35.3(5)	1.190(4)	2.789(9)	0.11(1)	15.0(6)	2.049(5)	0.31(1)	85.0(7)	0.496(9)	1.260(9)	7.8(8)
Ae40 4	0.415(3)	0.438(4)	0.13(1)	34.8(8)	1.206(5)	2.787(8)	0.11(1)	18.6(9)	2.085(9)	0.31(1)	81.4(8)	0.484(9)	1.450(9)	8.0(11)
Ae40 20	0.420(3)	0.450(3)	0.10(1)	35.7(5)	1.185(3)	2.786(9)	0.11(1)	19.0(9)	2.055(7)	0.32(1)	81.0(8)	0.494(10)	1.324(11)	7.9(9)
Ae45 1	0.415(3)	0.425(3)	0.06(1)	40.3(5)	1.180(4)	2.768(6)	0.11(1)	20.6(10)	2.006(9)	0.31(1)	79.4(10)	0.440(9)	1.315(11)	8.1(8)
Ae50 1	0.414(4)	0.416(5)	0.05(2)	41.9(14)	1.174(7)	2.765(10)	0.09(3)	21.8(14)	2.027(9)	0.27(2)	78.3(12)	0.519(9)	1.437(12)	8.5(9)
	0.414(3)	0.420(3)	0.08(1)	41.0(5)	1.183(4)	2.786(7)	0.08(3)	20.9(9)	2.043(8)	0.32(1)	79.1(9)	0.484(9)	1.408(12)	7.7(11)
Ae50/20/700	0.420(4)	0.429(3)	0.10(2)	42.0(7)	1.197(5)	2.758(7)	0.10(2)	20.1(8)	2.016(8)	0.32(2)	79.9(8)	0.455(11)	1.389(11)	8.0(11)
Ae50_leng	0.413(6)	0.427(7)	0.07(3)	41.4(11)	1.177(9)	2.771(11)	0.10(1)	23.4(23)	1.993(8)	0.24(2)	76.6(19)	0.493(12)	1.396(11)	10.1(12)
Ae55 1	0.423(2)	0.419(4)	0.09(1)	45.5(9)	1.199(6)	2.788(9)	0.08(2)	20.6(12)	2.004(10)	0.36(2)	79.4(9)	0.452(11)	1.371(9)	8.7(11)
Ae60 1	0.408(3)	0.407(2)	0.11(1)	54.1(6)	1.165(5)	2.762(8)	0.15(2)	24.1(15)	1.967(10)	0.36(2)	75.9(9)	0.461(10)	1.333(10)	6.3(13)
Ae60 2	0.411(3)	0.393(3)	0.10(2)	53.5(6)	1.173(4)	2.797(13)	0.10(2)	23.8(18)	1.976(8)	0.36(2)	76.2(17)	0.462(12)	1.369(11)	6.3(11)
Ae60 3	0.403(4)	0.390(3)	0.08(2)	54.1(9)	1.177(8)	2.779(9)	0.09(1)	24.1(15)	2.009(12)	0.28(3)	75.9(13)	0.473(11)	1.301(9)	6.8(15)
Ae60 4	0.406(4)	0.414(3)	0.12(2)	54.2(9)	1.170(6)	2.774(8)	0.13(2)	28.3(13)	1.986(10)	0.36(2)	71.7(12)	0.468(9)	1.272(9)	6.7(15)
Ae60 20	0.408(6)	0.396(2)	0.08(2)	52.6(7)	1.183(5)	2.761(9)	0.08(3)	21.8(16)	2.011(12)	0.39(2)	78.2(15)	0.488(8)	1.307(8)	6.8(14)
Ae70/1/700	0.410(6)	0.375(3)	0.11(3)	62.4(7)	1.177(8)	2.786(12)	0.08(4)	34.1(17)	1.967(11)	0.38(3)	65.9(13)	0.461(9)	1.314(9)	6.6(15)
Ae75/1/700	0.405(5)	0.367(2)	0.06(1)	68.3(11)	1.165(7)	2.741(8)	0.12(2)	34.5(14)	1.937(11)	0.25(3)	65.5(12)	0.567(11)	1.433(12)	5.1(14)
Ae75/2/500	0.397(3)	0.363(2)	0.10(1)	69.3(4)	1.171(5)	2.756(8)	0.11(3)	38.7(21)	1.949(15)	0.40(3)	61.3(18)	0.464(11)	1.346(11)	5.9(12)
Ae75/4/780	0.406(3)	0.354(4)	0.09(1)	68.1(11)	1.169(6)	2.792(15)	0.10(1)	37.3(22)	1.973(21)	0.36(3)	62.7(18)	0.470(10)	1.384(9)	5.9(14)
Ae75/5/700	0.405(3)	0.367(2)	0.07(1)	67.8(5)	1.163(5)	2.768(7)	0.12(2)	39.1(15)	1.966(11)	0.32(2)	60.9(14)	0.524(11)	1.371(9)	4.7(13)
Ae75/20/700	0.404(4)	0.370(2)	0.10(2)	67.7(4)	1.170(5)	2.734(7)	0.11(2)	34.5(13)	1.925(12)	0.35(2)	65.5(14)	0.485(10)	1.380(10)	5.5(14)
Ae75/21/700	0.398(5)	0.370(3)	0.09(2)	68.3(3)	1.181(3)	2.745(6)	0.15(1)	37.0(31)	1.886(9)	0.31(2)	63.0(25)	0.421(11)	1.434(10)	4.9(12)
Ae80/1/700	0.405(5)	0.334(2)	0.07(3)	75.9(5)	1.150(7)	2.790(15)	0.05(1)	37.9(18)	1.902(14)	0.37(3)	62.1(16)	0.502(8)	1.276(9)	4.0(11)
Ae85/1/700	0.400(4)	0.340(3)	0.04(1)	76.9(5)	1.177(8)	2.789(6)	0.13(1)	39.1(12)	1.842(14)	0.35(2)	60.9(13)	0.485(9)	1.277(9)	3.6(7)
Ae90/11	0.401(3)	0.312(3)	0.06(2)	91.7(4)	1.126(11)	2.778(11)	0.17(3)	57.2(15)	1.782(12)	0.30(2)	42.8(14)	–	–	–
Ae90/13/700	0.396(3)	0.322(3)	0.08(3)	88.3(6)	1.142(13)	2.743(15)	0.18(3)	50.5(26)	1.793(9)	0.14(3)	49.5(21)	–	–	–
Ae90/20/700	0.400(3)	0.326(3)	0.07(2)	91.4(3)	1.148(9)	2.766(12)	0.22(3)	55.9(21)	1.809(8)	0.38(4)	44.1(18)	–	–	–
Ae95/1/700	0.397(3)	0.319(3)	0.10(3)	91.6(4)	1.119(8)	2.779(11)	0.18(3)	58.2(14)	1.796(9)	0.25(4)	41.8()	–	–	–
Ae100/Ff	0.388(4)	0.283(4)	0.053(8)	100	–	–	–	–	–	–	–	–	–	–
Ae100/7/700	0.399(4)	0.290(4)	0.069(9)	100	–	–	–	–	–	–	–	–	–	–
Ae100/19/6500	0.397(4)	0.288(3)	0.078(8)	100	–	–	–	–	–	–	–	–	–	–

Notes: Abbreviations: IS = Isomer shift (mm/s), QS = quadrupole splitting (mm/s), sigma = Gaussian width, A = proportion of iron on a specific site, A* = relative proportion of Fe^{2+} within the Fe^{2+} quadrupole splitting distribution. All refinements were made on thin-limit spectra and imply a underlying Lorentzian full width at half maximum of 0.196 mm/s.

as the quadrupole splitting of Fe^{3+} (Fig. 8b) show some variations with the amount of aegirine component indicating small but significant variations in local electronic/geometric environments. In hedenbergite itself, the quadrupole splitting of Fe^{3+} is high, suggesting distorted oxygen environments around the Fe^{3+} cations. As the amount of the aegirine component increases, a very pronounced decrease of ΔE_Q is observed (up to about 25 mol% aegirine) after which there is a well-defined almost linear decrease of ΔE_Q (inset in Fig. 8b).

Figure 8c shows the evolution of the Fe^{2+} QSDs along the hedenbergite–aegirine solid-solution series. Two characteristics are evident here. First, the appearance of the Fe^{2+} QSD is distinctly bimodal. At intermediate compositions, the two Fe^{2+} components are clearly separated showing minimal overlap. As the mixed crystals show *C*2/*c* symmetry and Fe is not found on the M2 site, we have to assign both components to the crystal-

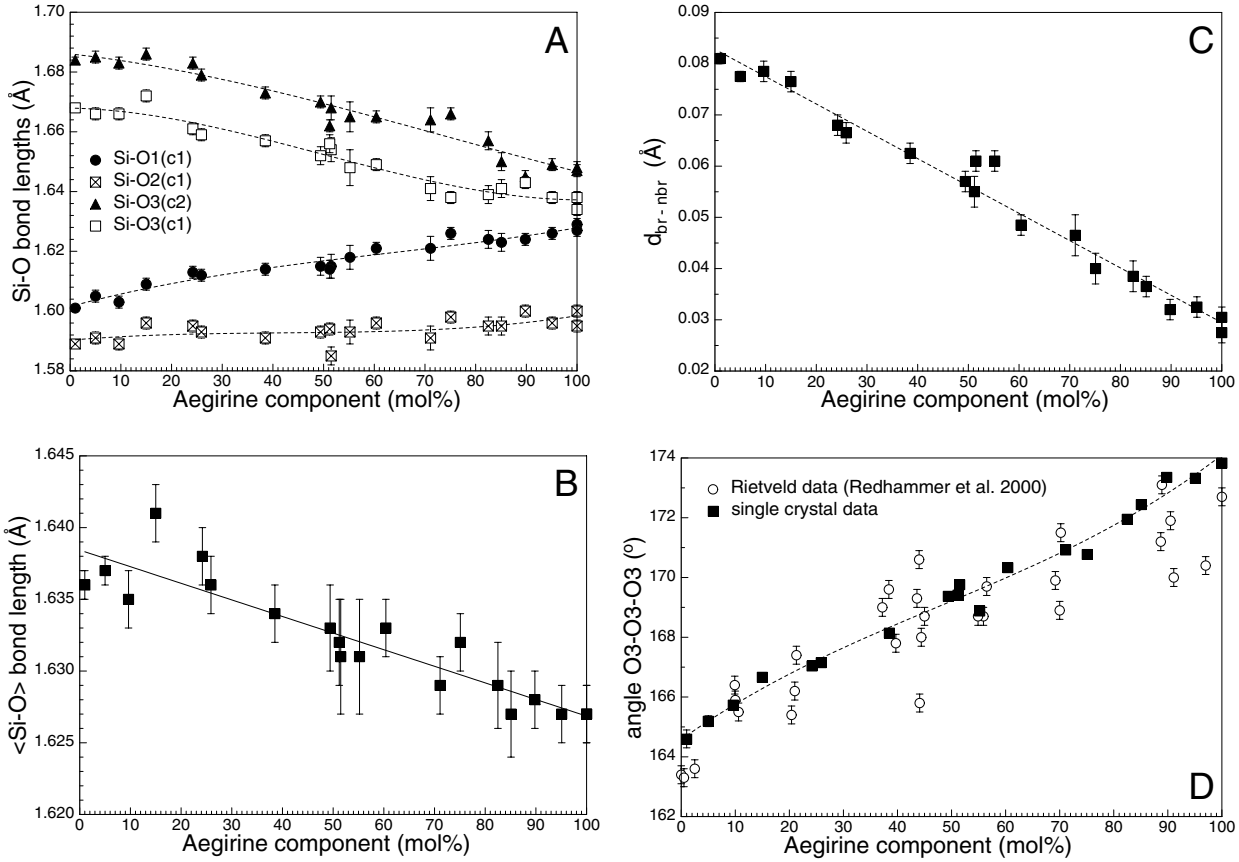

FIGURE 6. Structural parameters for the tetrahedral site of synthetic clinopyroxenes across the hedenbergite–aegirine solid-solution series as a function of the aegirine component content at 298 K: (**a**) individual Si-O bond lengths; (**b**) averaged Si-O bond lengths; (**c**) difference between average bridging and non-bridging Si-O bond lengths; and (**d**) change of the tetrahedral bridging (kinking) angle O3-O3-O3. Error bars are smaller than the symbols if not visible. Lines fitted to the data are guides to the eye.

lographic M1 site. In the following, the Fe^{2+}QSD component with the smaller quadrupole splitting will be denoted as Fe^{2+}-S, and the one with the larger quadrupole splitting Fe^{2+}-L. Second, the relative intensities of the two components are changing with chemical composition. In samples with a low aegirine content, the Fe^{2+}-S component dominates, whereas in aegirine-rich samples the Fe^{2+}-L component dominates. At intermediate compositions, the two components have nearly equal weights. Hedenbergite itself contains only the Fe^{2+}-S component. Besides the changes in the relative proportions of the two QSD components, the Fe^{2+} isomer shift, which is assumed to be the same for both sub-components, remains almost constant with a small tendency to decrease with increasing amount of the aegirine component (Fig. 8d). Redhammer et al. (2000) found in their Lorentzian-shape-based refinements that δ of the three individual Fe^{2+} doublets are identical within estimated standard deviations. The same was observed in the present study in refinements in which a coupling between δ and ΔE_Q was used/allowed. Here the differences in the δ values of the two Fe^{2+} sub-components are smaller than 0.005 mm/s. Although the overall changes in the isomer shift with chemical composition are small, those of the Fe^{2+}-S component especially for ΔE_Q are large (Fig. 8e). It decreases distinctly from ~2.26 mm/s in hedenbergite down to ~1.80 mm/s for aegirine-rich compositions, simultaneously the Fe^{2+}-L component shows a moderate increase from ~2.63 toward ~2.77 mm/s at intermediate compositions and remains almost constant afterward (inset in Fig. 8e). Similar behavior was found by Dollase and Gustafson (1982) in their model with two Fe^{2+} doublets. ^{57}Fe Mössbauer parameters for the Fe^{n+} range between ~0.42 and 0.58 mm/s for δ and between ~1.27 and ~1.66 mm/s for ΔE_Q. For both parameters, there is a slight negative correlation with the aegirine content of the samples, but the spread in the data is too large to deduce significant results. However, it is evident that the relative amount of Fe in the so-called Fe^{n+} state is highest in the intermediate compounds (up to 10% of total Fe) and decreases toward aegirine-poorer and aegirine-richer compositions (Fig. 8f). This finding means that the highest probability for the presence of mixed valence Fe occurs near an Fe^{2+}:Fe^{3+} ratio of 1:1.

Temperature dependent Mössbauer spectroscopy (80–700 K). Recording Mössbauer spectra for a given composition as a function of temperature (here 80 to 700 K) was done: (1) to prove the assignment of the weak third generalized QSD-site to fast electron hopping between Fe^{2+} and Fe^{3+}; and (2) to check for any variations in relative proportions of the two Fe^{2+} components Fe^{2+}-S and Fe^{2+}-L. Proving the first point requires an

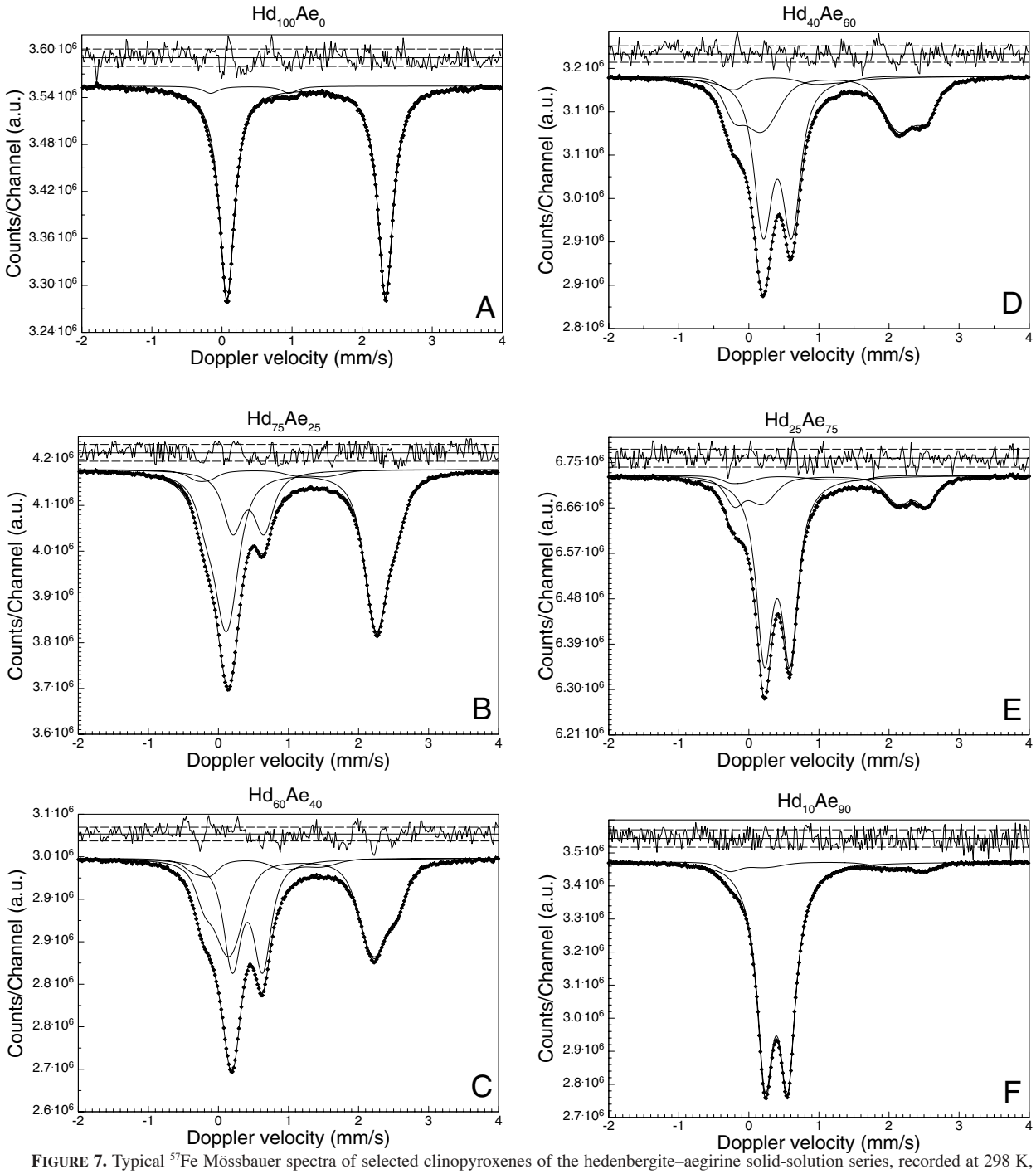

FIGURE 7. Typical ^{57}Fe Mössbauer spectra of selected clinopyroxenes of the hedenbergite–aegirine solid-solution series, recorded at 298 K, and evaluated with a quadrupole splitting distribution approach for Fe^{2+} on M1: (**a**) hedenbergite sample hed06; (**b**) composition ($Hd_{75}Ae_{25}$) sample ae2521; (**c**) composition ($Hd_{60}Ae_{40}$) sample ae401; (**d**) composition ($Hd_{40}Ae_{60}$) sample ae601; (**e**) composition ($Hd_{25}Ae_{75}$) sample ae751; and (**f**) composition ($Hd_{10}Ae_{90}$) sample ae9020.

increase in the relative intensity of this third generalized QSD-site with temperature (and its absence at low temperatures). For the latter point, changes in the relative proportions of the two Fe^{2+} subcomponents of the Fe^{2+} site would argue against an assignment of these subcomponents to different discrete NNN configurations. In fact, the appearance of the Mössbauer spectra for a given composition changes in a very pronounced way as a function of temperature. In Figures 9, 10, and 11,[2] selected ^{57}Fe Mössbauer spectra at different temperatures are shown for the compositions $Hd_{75}Ae_{25}$, $Hd_{50}Ae_{50}$, and $Hd_{25}Ae_{75}$, respectively. The variations of hyperfine parameters with temperature for the above-mentioned compositions are displayed in Figures 12,

[2] See earlier footnote about deposit items.

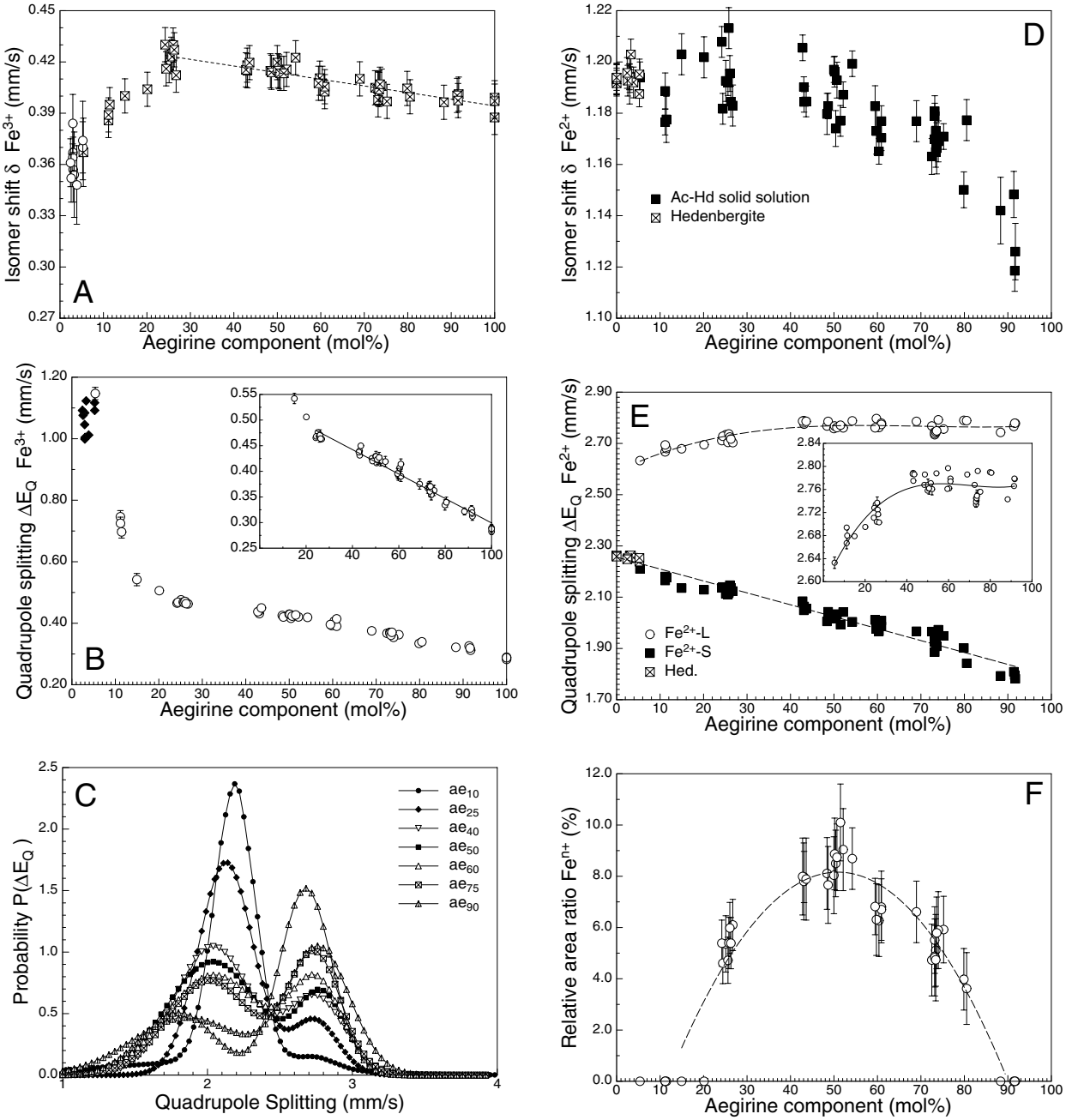

FIGURE 8. Variation of ^{57}Fe Mössbauer hyperfine parameters within the hedenbergite–aegirine $CaFe^{2+}Si_2O_6$–$NaFe^{3+}Si_2O_6$ solid-solution series at 298 K: (**a** and **b**) Isomer shift and quadrupole splitting of Fe^{3+}; (**c**) evolution of the Fe^{2+} quadrupole splitting distribution; (**d**) isomer shift of Fe^{2+}; (**e**) quadrupole splitting of the two Fe^{2+} QSD components with the inset showing the variation of the Fe^{2+}-L component on an enlarged scale; and (**f**) relative amount of Fe in the Fe^{n+} state at 298 K. Error bars are smaller than the symbols if not visible. Lines fitted to the data are guides to the eye.

13, and 14[2]. Table 6 compiles the ^{57}Fe Mössbauer data. In what follows, only the intermediate composition $Hd_{50}Ae_{50}$ will be discussed in detail.

It is evident that the appearance of ^{57}Fe Mössbauer spectra for sample $Hd_{50}Ae_{50}$ changes significantly with increasing temperature (Fig. 10). These changes mainly concern the Fe^{2+} resonance absorption contribution, evidently observable at the Fe^{2+} line at ~2.8 mm/s. At low temperatures, an asymmetric broadening is present at the low-velocity (left) side of the 2.8 mm/s line (Figs. 10a and 10b), but at high temperatures (T > 300 K), this asymmetry is found at the high-velocity side (Figs. 10e and 10f). Around room temperature, a distinct bimodal character is present (Fig. 10c for T = 250 K). It is also evident that the spectral resolution is reduced with increasing temperature, which is mainly due to reduced splitting of the low- and high-velocity lines of the Fe^{2+} quadrupole components. At 250

K, an additional resonance absorption contribution appears that is ascribed to Fe^{n+}. Around room temperatures, this component is distinctly asymmetric because of different isomer shift values of the underlying sub-components (expressed by a large coupling between isomer shift and quadrupole splitting with δ and ΔE_Q values close to those of ionic Fe^{2+} and Fe^{3+}), but it becomes more symmetric at high temperatures because the isomer shifts of the sub-component approach the same value. This observation means that the distribution of isomer shift values becomes more discrete as does the distribution of the Fe^{n+} quadrupole splitting thereby moving toward values intermediate to pure Fe^{2+} and Fe^{3+}. Once again, it is noted that the coupling between δ and ΔE_Q has no physical meaning, but is a fitting technique to produce a distribution of ΔE_Q with a corresponding distribution of δ. The visual changes in the appearance of spectra, which have been demonstrated to be fully reversible, are due to evident changes in ^{57}Fe hyperfine parameters and relative area fractions of individual Fe components.

The isomer shift for Fe^{3+} in ($Hd_{50}Ae_{50}$) decreases steadily and almost linearly with Fe^{3+}, whereas for Fe^{2+}, a slight non-linearity is observed. Principally the isomer shift consists of a contribution arising from the s-electron density at the Fe nucleus, the intrinsic isomer shift δ_I, and a contribution arising from the non-zero mean square velocity $\langle v^2 \rangle$, the so-called second-order Doppler shift δ_{SOD}. The latter contribution shows distinct temperature dependence, whereas the δ_I is almost temperature independent (De Grave and Van Alboom 1991; Van Alboom et al. 1993; Eeckhout and De Grave 2003a, 2003b). At 250 K, additional resonance absorption appears in the spectrum of $He_{50}Ae_{50}$, which shows average δ values only slightly larger than those found for pure Fe^{3+} (Fig. 13a). With increasing temperature, however, the isomer shift of this additional third QSD component increases and approaches values intermediate between Fe^{2+} and Fe^{3+}. Above ~550 K, it is almost ideally intermediate between the values of Fe^{2+} and Fe^{3+} (solid line in Fig 13a). This behavior is proof that the third generalized site can be assigned to thermally activated electron transfer between Fe^{2+} and Fe^{3+}.

The quadrupole splitting of Fe^{2+} generally is sensitive to changes in temperature through the valence term contribution, whereas the lattice terms exhibit only very small temperature dependence as a result of the thermal expansion of the lattice. However, the latter can be considered as constant to a good approximation. Depending on the magnitude of the energy gap between the lower Fe^{2+} ^5D energy levels, the valence term may vary rapidly (Van Alboom et al. 1993). Thereby weak temperature dependencies correlate with large splittings of the lower energy

TABLE 6. ^{57}Fe Mössbauer parameters of the synthetic clinopyroxenes for the hedenbergite $CaFe^{2+}Si_2O_6$–aegirine $NaFe^{3+}Si_2O_6$ solid-solution series as a function of temperature

		Fe^{3+}				Fe^{2+}							Fe^{n+}		
Sample	*T*	δ	QS	sigma	A	IS	QS-L	sigma	A*	QS-S	sigma	A*	<IS>	<QS>	A
Ae100F2f	80	0.489(4)	0.325(6)	0.03(2)	100	–	–	–	–	–	–	–	–	–	–
Ae100F2f	100	0.486(3)	0.322(7)	0.02(2)	100	–	–	–	–	–	–	–	–	–	–
Ae100F2f	150	0.466(4)	0.317(5)	0.02(1)	100	–	–	–	–	–	–	–	–	–	–
Ae100F2f	175	0.451(4)	0.317(6)	0.03(2)	100	–	–	–	–	–	–	–	–	–	–
Ae100F2f	200	0.442(3)	0.313(5)	0.02(2)	100	–	–	–	–	–	–	–	–	–	–
Ae100F2f	225	0.428(3)	0.311(6)	0.02(2)	100	–	–	–	–	–	–	–	–	–	–
Ae100F2f	250	0.416(3)	0.307(4)	0.03(2)	100	–	–	–	–	–	–	–	–	–	–
Ae100F2f	298	0.388(4)	0.303(5)	0.02(2)	100	–	–	–	–	–	–	–	–	–	–
Ae100F2f	325	0.373(4)	0.301(5)	0.03(2)	100	–	–	–	–	–	–	–	–	–	–
Ae100F2f	350	0.355(4)	0.296(6)	0.02(2)	100	–	–	–	–	–	–	–	–	–	–
Ae100F2f	375	0.339(3)	0.295(5)	0.02(2)	100	–	–	–	–	–	–	–	–	–	–
Ae100F2f	400	0.321(4)	0.295(5)	0.03(2)	100	–	–	–	–	–	–	–	–	–	–
Ae100F2f	425	0.305(4)	0.291(6)	0.03(3)	100	–	–	–	–	–	–	–	–	–	–
Ae100F2f	450	0.291(4)	0.290(6)	0.03(2)	100	–	–	–	–	–	–	–	–	–	–
Ae100F2f	475	0.274(3)	0.288(5)	0.03(2)	100	–	–	–	–	–	–	–	–	–	–
Ae100F2f	500	0.256(4)	0.285(6)	0.03(2)	100	–	–	–	–	–	–	–	–	–	–
Ae100F2f	525	0.239(4)	0.282(5)	0.03(2)	100	–	–	–	–	–	–	–	–	–	–
Ae75_20b	80	0.502(2)	0.383(3)	0.13(1)	74.2(3)	1.277(2)	3.100(8)	0.13(1)	78.1(7)	2.453(7)	0.28(1)	21.9(8)	–	–	–
Ae75_20b	100	0.499(3)	0.382(2)	0.10(1)	74.4(3)	1.274(2)	3.079(9)	0.10(1)	75.0(8)	2.394(5)	0.25(1)	25.0(9)	–	–	–
Ae75_20b	150	0.479(3)	0.376(4)	0.08()	75.8(3)	1.252(3)	3.040(7)	0.12(1)	69.3(9)	2.224(7)	0.29(1)	30.7(11)	–	–	–
Ae75_20b	175	0.468(5)	0.375(4)	0.08()	74.4(4)	1.241(3)	3.008(8)	0.12(1)	66.6(9)	2.198(7)	0.30(1)	33.4(12)	–	–	–
Ae75_20b	200	0.457(4)	0.374(4)	0.07(1)	74.7(3)	1.227(3)	2.967(7)	0.11(1)	61.3(9)	2.142(11)	0.39(2)	38.7(10)	–	–	–
Ae75_20b	250	0.428(3)	0.369(5)	0.06(1)	75.0(5)	1.197(4)	2.844(8)	0.12(2)	50.6(7)	1.986(6)	0.20(1)	49.4(8)	–	–	–
Ae75_20b	298	0.405(4)	0.367(4)	0.07(1)	68.4(7)	1.179(6)	2.739(8)	0.07(1)	41.8(8)	1.939(8)	0.36(2)	58.2(9)	0.463(6)	1.367(12)	4.8(8)
Ae75_20b	295	0.404(3)	0.361(6)	0.10(2)	71.7(7)	1.173(5)	2.709(8)	0.18(2)	44.3(8)	1.908(8)	0.23(3)	55.7(12)	0.463(6)	1.349(13)	4.7(8)
Ae75_20b	296	0.407(4)	0.371(4)	0.08(2)	67.8(6)	1.166(8)	2.749(11)	0.11(1)	38.8(11)	1.909(9)	0.29(3)	61.2(13)	0.500(5)	1.365(11)	5.8(9)
Ae75_20b	323	0.387(7)	0.360(4)	0.07(3)	65.0(9)	1.140(8)	2.697(7)	0.15(1)	33.5(15)	1.785(12)	0.26(2)	66.5(12)	0.543(7)	1.183(12)	10.0(11)
Ae75_20b	373	0.357(7)	0.357(3)	0.06(2)	63.7(9)	1.088(9)	2.526(7)	0.14(1)	20.2(11)	1.656(15)	0.28(2)	79.8(15)	0.582(6)	1.093(11)	12.2(12)
Ae75_20b	423	0.329(6)	0.351(3)	0.09(2)	59.8(9)	1.049(8)	2.347(7)	0.10(1)	11.3(17)	1.567(10)	0.28(3)	88.7(15)	0.593(7)	0.993(14)	18.5(8)
Ae75_20b	473	0.293(5)	0.347(7)	0.09(2)	58.2(10)	0.957(5)	–	–	0.0	1.446(9)	0.37(3)	100	0.589(8)	0.756(12)	21.5(8)
Ae75_20b	523	0.267(4)	0.339(7)	0.11(2)	58.2(9)	0.863(9)	–	–	0.0	1.283(13)	0.26(3)	100	0.543(6)	0.805(13)	20.5(9)
Ae75_20b	573	0.237(5)	0.338(8)	0.11(2)	50.0(11)	0.793(8)	–	–	0.0	1.388(15)	0.25(3)	100	0.505(6)	0.742(11)	21.8(11)
Ae50_20b	85	0.514(3)	0.447(5)	0.09(1)	48.5(6)	1.287(3)	3.065(7)	0.09(2)	49.0(12)	2.671(8)	0.28(2)	51.0(11)	–	–	–
Ae50_20b	100	0.509(4)	0.448(6)	0.08(1)	48.4(6)	1.280(5)	3.055(8)	0.09(1)	48.9(12)	2.641(8)	0.30(2)	51.1(10)	–	–	–
Ae50_20b	125	0.500(5)	0.441(6)	0.09(1)	48.9(5)	1.274(5)	3.045(8)	0.09(1)	45.1(11)	2.614(7)	0.31(2)	54.9(12)	–	–	–
Ae50_20b	150	0.490(4)	0.441(5)	0.07(1)	49.1(6)	1.259(5)	3.034(8)	0.05(1)	42.6(12)	2.542(8)	0.31(2)	57.4(11)	–	–	–
Ae50_20b	175	0.477(3)	0.432(4)	0.06(1)	49.2(5)	1.251(4)	3.000(7)	0.06(2)	37.2(21)	2.465(16)	0.35(3)	62.8(18)	–	–	–
Ae50_20b	200	0.468(5)	0.431(5)	0.07(1)	49.1(6)	1.230(5)	2.967(9)	0.08(2)	39.0(14)	2.359(9)	0.30(2)	61.0(12)	–	–	–

Note: Abbreviations: see Table 5.

TABLE 6.—*Continued*

	Fe^{3+}					Fe^{2+}							Fe^{n+}		
Sample	T	δ	QS	sigma	A	IS	QS-L	sigma	A*	QS-S	sigma	A*	<IS>	<QS>	A
Ae50_20b	225	0.455(3)	0.429(3)	0.10(1)	45.6(6)	1.224(3)	2.944(9)	0.06(3)	36.3(12)	2.331(12)	0.35(3)	63.7(13)	0.441(6)	1.453(8)	2.4(13)
Ae50_20b	250	0.441(5)	0.426(5)	0.07(1)	44.6(6)	1.211(5)	2.878(9)	0.08(2)	28.2(12)	2.206(9)	0.32(2)	71.8(13)	0.419(7)	1.347(9)	5.3(11)
Ae50_20b	298	0.416(6)	0.421(5)	0.06(1)	43.1(7)	1.187(5)	2.761(10)	0.07(1)	22.9(13)	2.042(8)	0.28(2)	77.1(12)	0.470(6)	1.382(9)	8.0(10)
Ae50_20b	298	0.415(5)	0.429(5)	0.08(1)	41.3(6)	1.196(6)	2.768(10)	0.09(2)	19.2(12)	2.034(9)	0.33(2)	80.8(13)	0.434(8)	1.355(9)	8.9(8)
Ae50_20b	298	0.413(5)	0.423(5)	0.07(1)	41.9(8)	1.193(5)	2.762(10)	0.09(2)	21.3(11)	2.032(9)	0.30(2)	78.7(13)	0.462(6)	1.370(10)	8.7(9)
Ae50_20b	325	0.397(3)	0.420(5)	0.10(1)	37.1(9)	1.164(5)	2.705(11)	0.08(3)	14.6(18)	1.904(7)	0.31(2)	85.4(13)	0.487(9)	1.237(8)	17.3(7)
Ae50_20b	350	0.386(5)	0.414(6)	0.10(1)	35.0(10)	1.139(6)	2.571(11)	0.08(2)	16.8(14)	1.804(9)	0.28(3)	83.2(12)	0.485(9)	1.164(8)	20.2(8)
Ae50_20b	375	0.376(6)	0.411(6)	0.11(1)	35.5(11)	1.114(6)	2.479(10)	0.08(1)	13.5(15)	1.726(10)	0.27(3)	86.5(14)	0.508(9)	1.196(8)	20.9(8)
Ae50_20b	405	0.367(5)	0.408(7)	0.12(1)	31.9(9)	1.103(5)	2.366(12)	0.16(2)	16.4(14)	1.668(11)	0.24(2)	83.6(14)	0.558(7)	1.099(9)	21.9(9)
Ae50_20b	425	0.347(5)	0.408(7)	0.15(1)	33.5(8)	1.060(5)	2.324(12)	0.10(2)	12.9(12)	1.629(12)	0.43(2)	87.1(12)	0.535(8)	1.063(11)	23.4(7)
Ae50_20b	450	0.338(6)	0.406(6)	0.11(1)	30.8(10)	1.048(6)	2.214(9)	0.15(2)	10.4(14)	1.562(11)	0.20(3)	89.6(12)	0.594(6)	1.038(10)	26.7(8)
Ae50_20b	475	0.323(5)	0.401(7)	0.14(1)	32.0(8)	1.013(7)	2.150(10)	0.10(2)	11.5(16)	1.548(12)	0.24(3)	88.5(11)	0.577(8)	0.996(10)	26.7(8)
Ae50_20b	500	0.313(5)	0.396(8)	0.13(1)	31.0(9)	0.977(6)	2.133(11)	0.10(2)	7.8(17)	1.508(14)	0.26(3)	92.2(16)	0.586(7)	0.904(12)	28.2(9)
Ae50_20b	525	0.294(6)	0.396(8)	0.13(1)	31.8(8)	0.967(7)	2.050(9)	0.10(3)	5.1(24)	1.451(12)	0.21(3)	94.9(15)	0.576(8)	0.834(10)	29.6(7)
Ae50_20b	550	0.286(6)	0.388(6)	0.12(1)	29.4(12)	0.933(7)	2.020(12)	0.10(4)	5.5(21)	1.450(12)	0.22(3)	94.5(11)	0.591(8)	0.830(12)	28.9(8)
Ae50_20b	600	0.255(5)	0.387(8)	0.12(1)	30.3(12)	0.894(6)	–	–	–	1.343(11)	0.25(3)	100	0.543(7)	0.742(11)	28.6(8)
Ae50_20b	650	0.221(6)	0.382(8)	0.18(1)	30.1(9)	0.801(7)	–	–	–	1.280(12)	0.25(2)	100	0.517(9)	0.661(12)	27.7(9)
Ae50_20b	700	0.185(6)	0.374(9)	0.21(1)	29.2(9)	0.769(7)	–	–	–	1.182(14)	0.27(3)	100	0.470(8)	0.624(11)	29.2(11)
Ae25_20b	80	0.518(3)	0.484(4)	0.13(1)	24.8(3)	1.308(3)	3.106(4)	0.10(2)	20.8(11)	2.768(3)	0.17(2)	79.2(11)	–	–	–
Ae25_20b	100	0.513(3)	0.486(4)	0.12(1)	25.0(3)	1.302(2)	3.080(4)	0.09(3)	24.0(23)	2.735(4)	0.16(2)	76.0(9)	–	–	–
Ae25_20b	150	0.498(3)	0.480(4)	0.12(1)	24.5(3)	1.280(3)	3.026(8)	0.09(2)	21.3(15)	2.630(5)	0.16(2)	78.7(14)	–	–	–
Ae25_20b	170	0.486(3)	0.480(4)	0.11(1)	24.3(3)	1.269(3)	2.990(7)	0.09(2)	22.8(15)	2.565(8)	0.15(2)	77.2(12)	–	–	–
Ae25_20b	200	0.472(3)	0.476(4)	0.11(1)	24.0(4)	1.252(3)	2.947(7)	0.09(1)	20.3(11)	2.492(7)	0.15(2)	79.7(12)	–	–	–
Ae25_20b	250	0.455(3)	0.474(7)	0.14(1)	20.5(5)	1.230(3)	2.879(9)	0.10(3)	15.9(21)	2.334(7)	0.19(2)	84.1(18)	0.464(8)	1.535(9)	4.2(11)
Ae25_20b	295	0.423(5)	0.467(8)	0.09(1)	15.4(9)	1.213(4)	2.737(9)	0.10(2)	12.0(9)	2.117(6)	0.20(1)	88.1(11)	0.454(9)	1.207(9)	10.4(9)
Ae25_20b	296	0.430(5)	0.471(4)	0.12(1)	21.1(5)	1.195(3)	2.725(5)	0.09(2)	13.7(8)	2.147(12)	0.17(1)	86.3(9)	0.515(7)	1.575(9)	6.0(8)
Ae25_20b	323	0.417(5)	0.456(5)	0.15(1)	21.6(8)	1.170(3)	2.686(7)	0.10(2)	8.7(9)	2.010(8)	0.22(1)	91.3(9)	0.496(8)	1.394(10)	13.0(9)
Ae25_20b	373	0.385(7)	0.470(9)	0.09(1)	17.4(11)	1.128(4)	2.465(13)	0.10(1)	6.4(7)	1.819(7)	0.19(1)	93.6(8)	0.556(9)	1.295(8)	20.2(8)
Ae25_20b	423	0.359(6)	0.461(11)	0.05(3)	16.4(6)	1.095(3)	2.265(18)	0.10(1)	5.3(9)	1.683(9)	0.17(1)	94.7(8)	0.630(7)	1.245(8)	23.3(10)
Ae25_20b	473	0.329(7)	0.457(8)	0.10(2)	15.2(10)	1.037(6)	–	–	–	1.584(12)	0.19(1)	100	0.590(6)	1.051(9)	22.1(9)
Ae25_20b	523	0.295(9)	0.447(11)	0.14(3)	11.0(25)	0.979(9)	–	–	–	1.484(14)	0.17(1)	100	0.564(7)	0.926(8)	25.7(8)
Ae25_20b	573	0.282(9)	0.451(14)	0.10(1)	13.3(24)	0.930(7)	–	–	–	1.382(15)	0.16(1)	100	0.569(7)	0.880(8)	23.3(10)
Hd1	80	–	–	–	–	1.307(3)	–	–	–	2.762(4)	0.02(1)	100	–	–	–
	100	–	–	–	–	1.307(4)	–	–	–	2.718(4)	0.02(1)	100	–	–	–
	150	–	–	–	–	1.278(4)	–	–	–	2.618(5)	0.02(1)	100	–	–	–
	175	–	–	–	–	1.268(3)	–	–	–	2.562(4)	0.02(1)	100	–	–	–
	200	–	–	–	–	1.248(4)	–	–	–	2.491(4)	0.02(1)	100	–	–	–
	225	–	–	–	–	1.228(4)	–	–	–	2.416(5)	0.02(2)	100	–	–	–
	250	–	–	–	–	1.217(4)	–	–	–	2.347(5)	0.03(1)	100	–	–	–
	298	–	–	–	–	1.193(5)	–	–	–	2.228(4)	0.02(2)	100	–	–	–
	325	–	–	–	–	1.165(4)	–	–	–	2.124(4)	0.03(1)	100	–	–	–
	350	–	–	–	–	1.147(4)	–	–	–	2.054(7)	0.03(1)	100	–	–	–
	375	–	–	–	–	1.127(3)	–	–	–	1.978(5)	0.02(2)	100	–	–	–
	400	–	–	–	–	1.109(4)	–	–	–	1.907(5)	0.02(1)	100	–	–	–
	425	–	–	–	–	1.090(4)	–	–	–	1.835(4)	0.03(2)	100	–	–	–
	450	–	–	–	–	1.076(5)	–	–	–	1.785(5)	0.02(1)	100	–	–	–
	475	–	–	–	–	1.057(4)	–	–	–	1.718(4)	0.01(2)	100	–	–	–
	500	–	–	–	–	1.038(4)	–	–	–	1.657(5)	0.03(2)	100	–	–	–

Note: Abbreviations: see Table 5.

levels arising from considerable deformations of the coordination octahedra, whereas for Fe^{2+} in regular octahedral coordination (small splittings of the lower Fe^{2+} energy levels) a large temperature dependence can be expected (Van Alboom et al. 1993). Such features actually are found for the two Fe^{2+} components in $Hd_{50}Ae_{50}$ (Fig. 13b). It is evident that up to ~350 K, the inner Fe^{2+} component shows a distinctly larger temperature dependence than the outer one, i.e., the difference between the quadrupole splittings of the two components increases between 80 and ~350 K. The Fe^{2+}-L thus not only shows smaller relative changes as a function of variable chemistry, but also as a function of variable temperature. The temperature variation of the Fe^{3+} quadrupole splitting is small (Fig. 13b), which goes along with the generally small sensitivity of Fe^{3+} to changes in temperature (due to a spherical electron distribution around the nucleus). The (average) quadrupole splitting of the third site, assigned to Fe^{n+}, is between the values of Fe^{2+} and Fe^{3+} and decreases with temperature in a manner similar to that of the Fe^{2+}-S component (Fig. 13b). A further important result of the temperature dependent Mössbauer spectroscopic investigations on $Hd_{50}Ae_{50}$ is that the amount of Fe^{n+} increases with temperature up to ~29% of total Fe (Fig. 13c). Above ~530 K, the amount of Fe^{n+} remains almost constant. At 80 K, the Fe^{2+}-L and Fe^{2+}-S components are equal in intensity in $Ae_{50}Hd_{50}$, whereas the Fe^{2+}-S component gains relative intensity as temperature is raised. At moderate temperatures (298 K), the Fe^{2+}-S component becomes dominant and at high temperatures, the Fe^{2+}-L component is absent or at least very low in intensity. The change in relative intensity of the two Fe^{2+} components is also evident by comparing the Fe^{2+} QSD curves extracted from the spectra recorded at different temperatures (Fig. 13d).

The changes of spectral features and ^{57}Fe hyperfine parameters with temperature for the mixed crystals with approximately $Hd_{75}Ae_{25}$ and $Hd_{25}Ae_{75}$ composition are similar to the ones described in some detail above. For both compounds, the

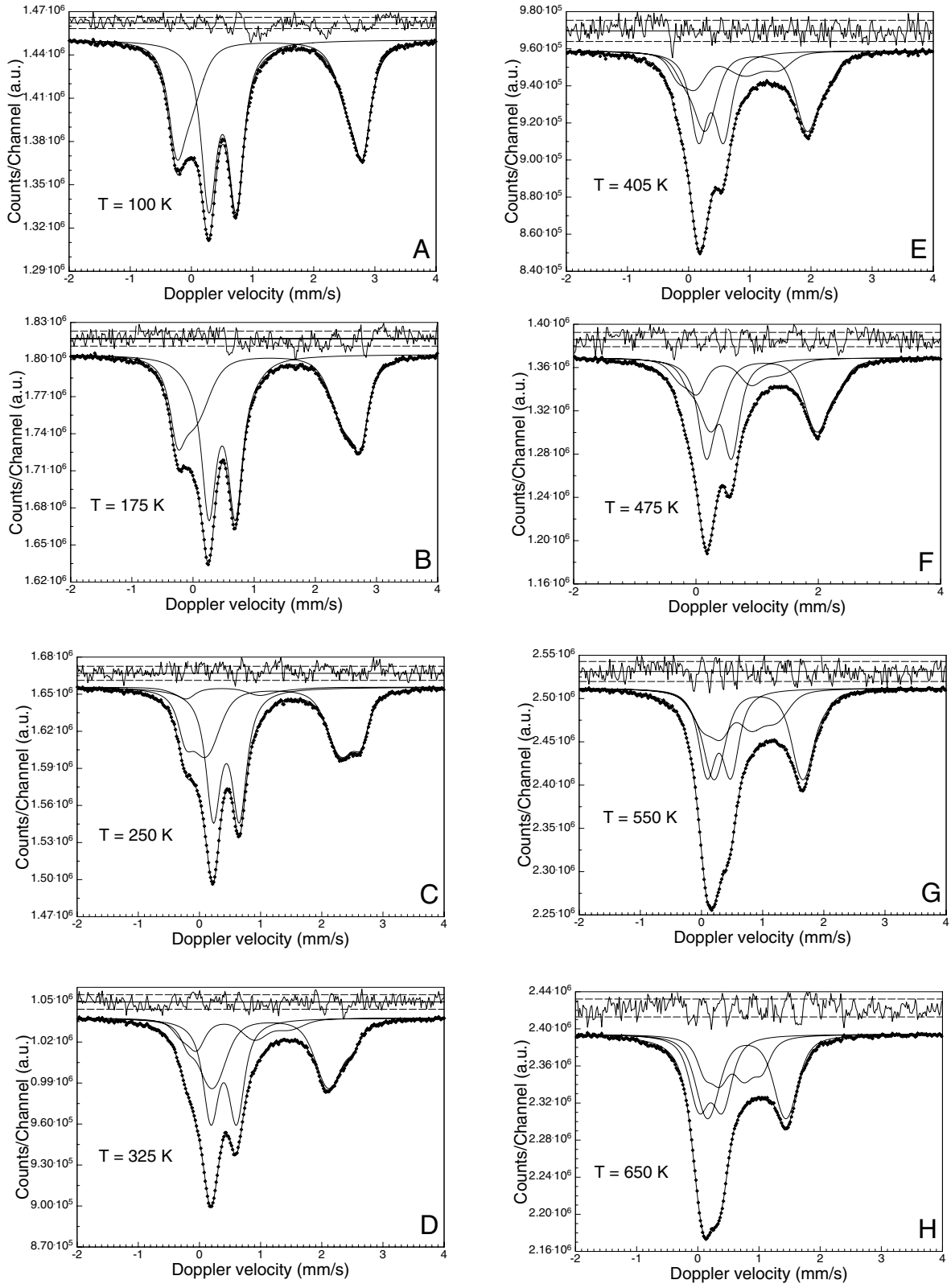

FIGURE 10. Typical ^{57}Fe Mössbauer spectra of sample Ae5020 ($Hd_{50}Ae_{50}$) recorded at different temperatures and evaluated with the quadrupole splitting distribution approach: (**a**) T = 100 K; (**b**) T = 175 K; (**c**) T = 250 K; (**d**) T = 325 K; (**e**) T = 405 K; (**f**) T = 475 K; (**g**) T = 550 K; and (**h**) T = 650 K.

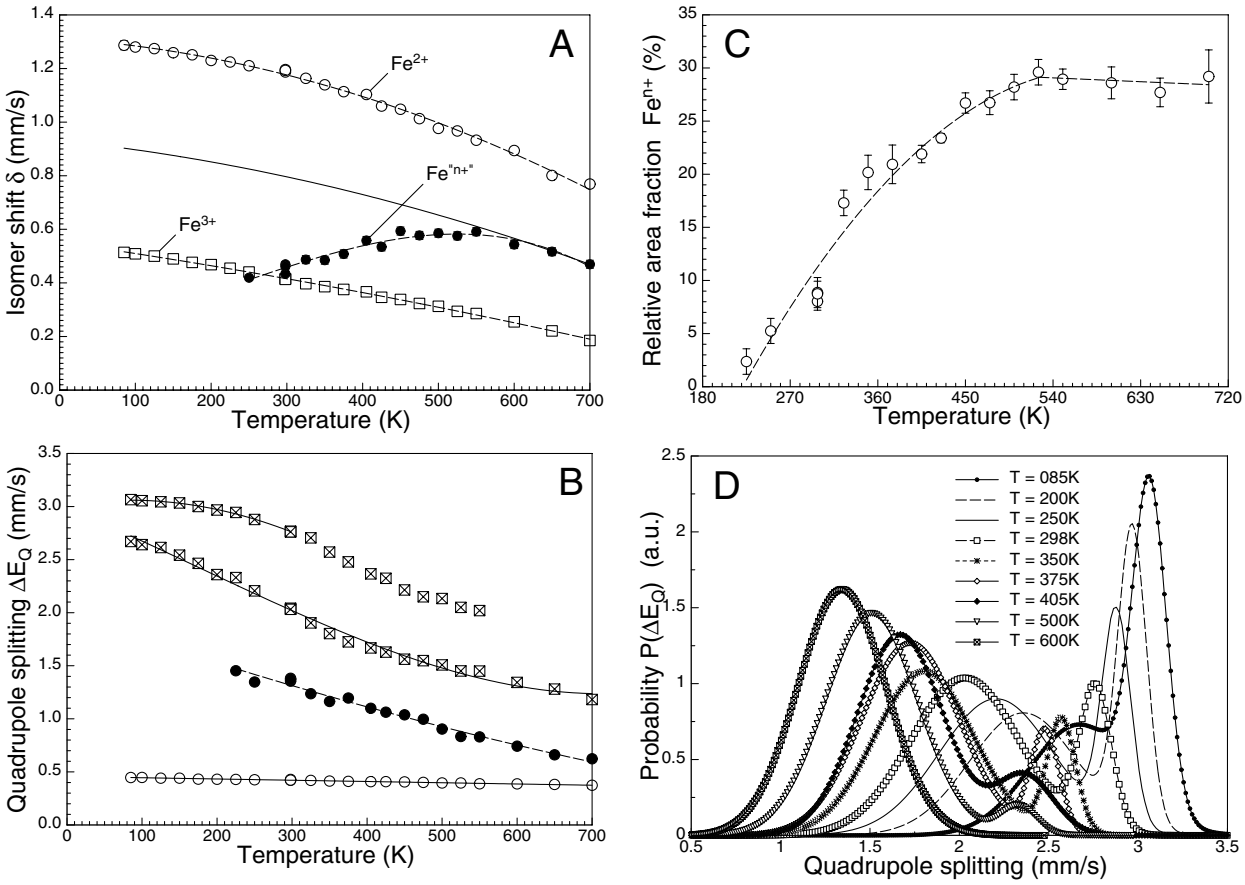

FIGURE 13. Variation of Mössbauer ^{57}Fe hyperfine parameters for sample ae5020 ($Hd_{50}Ae_{50}$) with temperature: (**a**) isomer shift for all Fe species; (**b**) quadrupole splitting for all Fe subcomponents; (**c**) fraction of Fe in the Fe^{n+} state (for total Fe = 100%); and (**d**) variation of Fe^{2+} quadrupole splitting distribution curves with temperature. Error bars are smaller than the symbols if not visible. Lines fitted to the data are guides to the eye.

isomer shift values of Fe^{2+} and Fe^{3+} show a smooth decrease with increasing temperature, and the first signs of the Fe^{n+} component appear at 250 K. As for the intermediate composition, the isomer shift of the Fe^{n+} component increases first with temperature, thereby approaching values intermediate between Fe^{2+} and Fe^{3+}. What is more, the relative proportions of the two Fe^{2+} components change significantly with temperature. Thus, in these two compounds, there also is fast electron hopping between Fe^{2+} and Fe^{3+} above 250 K, and the Fe^{2+} line broadening cannot be ascribed to a model with discrete NNN-configurations, as the relative proportion of such configurations must not change with temperature. For more details, the reader is referred to Figures 9, 11, 12, and 14, respectively.

Both pure hedenbergite and pure aegirine were also investigated as a function of temperature between 80 and 500 K to facilitate comparison with the compounds $Hd_{75}Ae_{25}$, $Hd_{50}Ae_{50}$, and $Hd_{25}Ae_{75}$. When plotting all isomer shift values for Fe^{3+} measured as a function of temperature for the solid-solution compounds and pure aegirine (Fig. 15a), it is evident that the temperature dependencies are very similar for all the samples. It may be concluded that the end-member aegirine shows a somewhat larger *T* dependence of δ as compared to the hedenbergite-rich compositions. The isomer shift values of Fe^{2+} also are close to each other (Fig. 15b), with a tendency of a somewhat larger *T* dependence for the sample richest in aegirine component $Hd_{25}Ae_{75}$. The absolute values of the Fe^{3+} quadrupole splitting are plotted in Figure 15c, and the changes relative to values at 80 K are depicted in Figure 15d. Here it is evident that the overall changes are small and quite similar to each other. In contrast, the temperature dependencies of the Fe^{2+} quadrupole splittings are large (Fig. 15e). Here, the absolute, as well as the relative, changes for the large QSD components Fe^{2+}-L are very similar to each other, and the temperature dependence can be described well by a common regression line. Common to all three solid-solution series compounds is the change in relative proportion of the two QSD components as a function of temperature. It is well established by the data of this study that at high temperatures, the component with the smaller quadrupole splitting is dominant (Fig. 15f). This change in relative Fe^{2+} proportions is most evident for sample $Hd_{25}Ae_{75}$ in which at low temperature the Fe^{2+}-L component is dominating. It is worth noting that linear regression lines fitted to the data for $Hd_{25}Ae_{75}$ and $Hd_{75}Ae_{25}$ join together at ~480 K for full occupancy of the Fe^{2+}-S component. Extrapolating the trend of the data for $Hd_{50}Ae_{50}$ below 400 K would also fit this common joining point quite well. However, for the intermediate composition there still is a population of the

Fe^{2+}-L component above ~480 K demonstrating some different behavior of the intermediate compound.

Discussion

The structural variations within the hedenbergite–aegirine solid solution are dominated by substitutions on the M1 site. The decrease of the *a* and *b* lattice parameters is ascribed to the $Fe^{2+} \rightarrow Fe^{3+}$ replacement. We assume that the increase of the *c* lattice parameter is not dominated by the replacement of Ca^{2+} by Na^{+}, but mainly is a reaction to the enhanced electrostatic repulsion between the highly charged Fe^{3+} cations. The non-linear behavior in the variation of *c* as a function of chemical composition may be ascribed to the non-linear variation of the Fe-Fe interatomic distance within the M1 chain, running parallel to **c**.

The reduction of tetrahedral kinking also can be assigned to structural changes within the M1 chain. As two coplanar M1 chains are interconnected by two tetrahedral chains, a stretching of the M1 chain in the c direction (increase of the *c* lattice parameter) results in a stretching of the tetrahedral chain. This is shown by the increase of the tetrahedral kinking angle O3-O3-O3 (Fig. 6f). The approach of the O3-O3-O3 tetrahedral bridging angle toward the value of a fully extended chain (180°) has a direct consequence on the coordination of the M2 site. Two of the four O3 oxygen atoms are moved toward the M2 cation as the tetrahedral chain becomes more extended, and the other two are moved away from the M2 cation. This movement results in the 6+2 coordination of M2 in aegirine. The slight increase of the M2-O1 and M2-O2 interatomic distances with increasing aegirine component is the result of the approach of the O1 and O2 oxygen atoms toward the M1 cation. In summary, structural changes within the tetrahedral and the M2 sites are adjustments to the changes induced on the M1 site by the $Fe^{2+} \rightarrow Fe^{3+}$ substitution.

The Mössbauer spectroscopic investigations on mixed crystals of the hedenbergite–aegirine series have shown that two Fe^{2+} components, distinctly different in their quadrupole splitting, can occur, even if only one crystallographic position is available to which these two main components have to be assigned. It is clear from the results that a multiple component model is necessary to model the Fe^{2+} resonance absorption contribution. Dollase and Gustafson (1982) used a two- and a three-doublet model, whereas we have—for the first time—applied a QSD model for refining the spectra. Best results were obtained by using two Gaussian components within the Fe^{2+} QSD. The appearance of these two Fe^{2+} components only can be explained in a plausible way by assuming the presence of two different groups of local electronic and/or geometric distortion environments (LDE). These LDEs are most probably due to different occupancies of the NNN sites to M1 by Fe^{2+} and Fe^{3+} and to M2 by Ca^{2+} and Na^{+}, respectively. Each M1 site has two neighboring M1 and three neighboring M2 sites. The pronounced change in the relative intensities of the two Fe^{2+} components as a function of temperature for a fixed chemical composition and the complete reversibility of this process, however, rules out that discrete NNN configurations are responsible. Furthermore, chemical zoning with a hedenbergite-rich and an aegirine-rich part can also be excluded on the basis of this argument.

Discrete NNN configurations of the M2 site were suggested as the cause of the Fe^{2+} line broadening in omphacite by Aldridge et al. (1978). Those authors adopted the model of Dowty and Lindsley (1973), who proposed that Fe^{2+} in the clinopyroxene M1 site yields different quadrupole doublets depending upon the occupancy of adjacent M2 sites. Aldridge et al. (1978) concluded that the Fe^{2+} resonance absorption is the sum of three discrete doublets corresponding to Fe^{2+}-(Ca, Na, Na), Fe^{2+}-(Ca, Ca, Na), and Fe^{2+}-(Ca, Ca, Ca) configurations. Dollase and Gustafson (1982) pointed out some weakness in this model, although they succeeded in reproducing the spectra with three doublets for Fe^{2+} and—by applying massive constraints—in finding peak component areas that are the same at both 298 and 80 K. The debatable point of this approach is that different electric field gradients should only result from the number of Ca^{2+} and Na^{+} cations on M2, but are assumed to depend on neither their spatial arrangement, nor on charge and size of the M2 cations, nor on the valence and size of the neighboring edge-sharing M1 cations (Dollase and Gustafson 1982). As structure refinements have shown, the $Fe^{2+}O_6$ octahedron is different from the $Fe^{3+}O_6$ octahedron in size and distortion. Certainly, distinct local rearrangements have to be expected locally in the M1 octahedral chain in the mixed crystals depending on whether M1 is occupied by Fe^{2+} or Fe^{3+}. Moreover, if the quadrupole splitting of Fe^{2+} is solely a function of the M2 site occupancy, then a given Fe^{2+}-(M2, M2, M2) configuration should be fairly rigid throughout the complete solid-solution series, which is not true for the samples studied here. In the QSD model of this study, the Fe^{2+}-S component changes its quadrupole splitting by ~0.46 mm/s at 298 K through the binary join. This also holds true if a model with three discrete Lorentzian shaped doublets for Fe^{2+} is used (Redhammer 1996). Again, distinct influences of ΔE_Q are present, due to the chemical variation in the coordination of the Fe^{2+} site, variations that are similar to those given by Dollase and Gustafson (1982) in their three doublet model. The change in ΔE_Q of the Fe^{2+}-S QSD component is numerically as large as the difference between the (Ca, Ca, Ca) and the (Ca, Ca, Na) configurations, which are assumed to have ΔE_Q values of about 1.8 and 2.2 mm/s, respectively (Aldridge et al. 1978). According to this result, the quadrupole splitting of hedenbergite agrees better with a (Ca,Ca,Na) configuration, which—of course—cannot be true. Substituting Fe^{2+} in hedenbergite by Mg^{2+} (Dollase and Gustafson 1982) or by Ni^{2+} (Redhammer 2001) without changing the M2 site composition lowers the ΔE_Q of Fe^{2+} on M1 by 0.38 down to 1.86 mm/s. This change is as large as the difference of 0.35–0.40 mm/s between the M2 site configurations of Aldridge et al. (1978) and implies that the occupancy of the M2 site is not more influencial in determining the ΔE_Q of Fe^{2+} on the M1 site than occupancy of neighboring edge-sharing M1 sites, which is responsible for the decrease of Fe^{2+} ΔE_Q in the $Ca(Fe^{2+}, Mg)Si_2O_6$ and $Ca(Fe^{2+}, Ni)Si_2O_6$ series. Thus, the NNN model with discrete M2 site configurations is not applicable to interpreting the Fe^{2+} absorption asymmetry in (hedenbergite–aegirine) clinopyroxenes.

At first glance, it is excluded that the line broadening and the changes in relative area fractions of the Fe^{2+} subcomponents are due to the appearance of thermally activated electron charge transfer between Fe^{2+} and Fe^{3+} as proposed

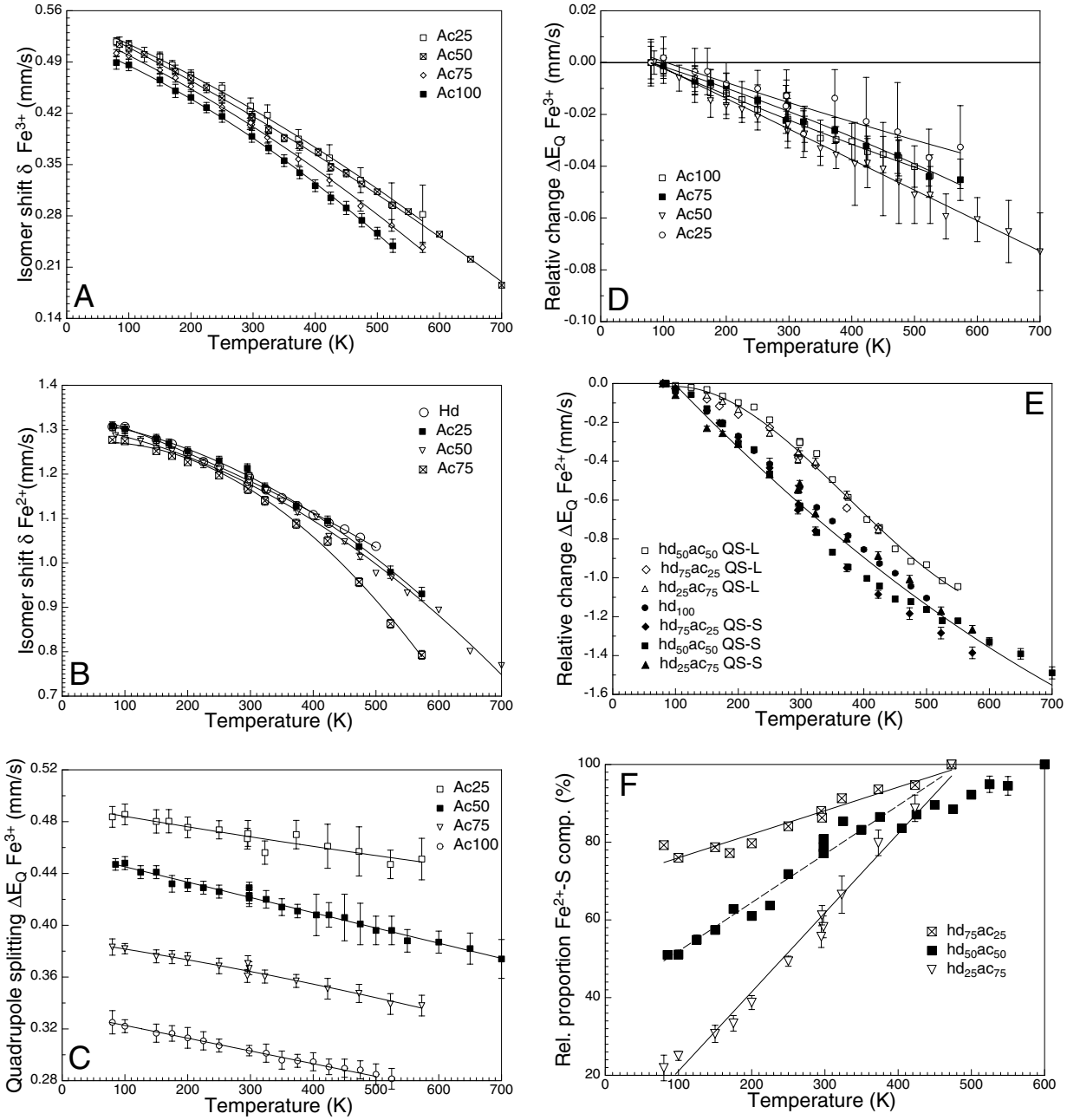

FIGURE 15. Variations of ^{57}Fe hyperfine parameters of the hedenbergite $CaFe^{2+}Si_2O_6$–aegirine $NaFe^{3+}Si_2O_6$ solid-solution series as a function of temperature: (**a**) Isomer shift of Fe^{3+}; (**b**) Isomer shift of Fe^{2+}; (**c**) Quadrupole splitting of Fe^{3+}; (**d**) Relative change of Fe^{3+} quadrupole splitting with respect to the values at 80 K; and (**e**) Relative change of the Fe^{2+} quadrupole splitting with respect to the values at 80 K. Lines represent fits to all the data of a group, Fe^{2+}-L, and Fe^{2+}-S, respectively.

by Amthauer and Rossman (1984). The spectral signature for this so-called electron hopping is different and appears in the velocity range of 1.0–1.2 mm/s at temperatures above 200 K in synthetic samples and is distinctly present at temperatures above 300 K. Moreover, as temperature increases, this QSD-site shows an increasing area contribution. Correspondingly, a decrease of the area contribution of participating Fe^{2+} and Fe^{3+} was observed, which can be seen as good evidence for electron delocalization. The basic structural requirements allowing electron hopping processes are given within the hedenbergite–aegirine series: an infinite zigzag chain of M1 octahedra, a common edge between neighboring M1 sites, and a relatively short interatomic distance between neighboring Fe-Fe pairs (Table 4). At temperatures at and slightly above 298 K we find states that are Fe^{2+}-like and Fe^{3+}-like in terms of their isomer shift and quadrupole splitting values, though with values for the isomer shift (and quadrupole splitting) that are slightly too low (Fe^{2+}) and too high (Fe^{3+}) as compared to pure

ionic divalent and trivalent oxidation states, respectively. As temperature increases, the ^{57}Fe hyperfine parameters approach values between those of Fe^{2+} and Fe^{3+}. This is a typical behavior of mixed valence Fe and also was described in detail in ilvaite $CaFe^{2+}_2Fe^{3+}(Si_2O_7/O/OH)$ by Litterst and Amthauer (1984).

It is proposed that the two different classes of Fe^{2+} ΔE_Q within the hedenbergite–aegirine solid-solution series represent two different types of electric field gradients. A similar explanation was considered previously by Dollase and Gustafson (1982) and by De Grave et al. (1998). Simply speaking, the electric field gradient is the sum of two principal components: (1) the lattice term arising from the deviation from cubic symmetry of the atoms surrounding the Fe atom; and (2) the valence term describing the deviation from cubic symmetry of the d-electrons (5 for Fe^{3+}, 6 for Fe^{2+}) of the Fe atom itself. To produce large differences in ΔE_Q for Fe^{2+}, either the lattice term or the valence term (or both) have to change markedly. Ingalls (1964) has shown that for slight distortions from octahedral symmetry (near the degeneracy of the orbital energy levels in t_{2g} and e_g), the valence term shows a very pronounced increase for finite temperatures due to a decrease in the thermal occupation of the t_{2g}-like orbitals, which are unoccupied at $T = 0$ K. At higher deviations from ideal octahedral symmetry, where this thermal occupancy is negligible, the valence-term contribution to the electric field gradient decreases due to increasing admixture of the unoccupied d-orbital into the occupied ligand orbitals. The lattice term, which is opposite in sign to the valence term, increases linearly with increasing octahedral distortion. Consequently, for sufficiently large distortions as usually observed in minerals, a negative correlation between quadrupole splitting and distortion is found for octahedral Fe^{2+} (Ingalls 1964; Dowty and Lindsley 1973). Because of the small overall site distortion of the M1 octahedron in hedenbergite, we can expect the following: (1) quadrupole splitting and distortion probably are correlated positively; and (2) even small changes in distortion from cubic symmetry will produce large changes in Fe^{2+} quadrupole splitting due to the valence-term contributions. As for Fe^{3+}, with its more or less symmetric spatial distribution of 3d electrons, the valence-term contribution to the electric field gradient is vanishing or low, so the compositional sensitivity of the lattice term across the hedenbergite–aegirine binary can be estimated. Over large parts of the solid-solution series, the ΔE_Q of Fe^{3+} stays constant. Above aegirine concentrations of ~20 mol%, the absolute numerical change is only ~0.22 mm/s and thus is much smaller than the one of Fe^{2+}. We agree with Dollase and Gustafson (1982) that a similarly small compositional sensitivity also accounts for the lattice-term contribution to ΔE_Q Fe^{2+}. Thus the contribution that dominates the large compositional as well as temperature dependent changes of Fe^{2+} ΔE_Q, is the valence term. Based on the considerations above, we assign the Fe^{2+}-S component in the Fe^{2+} QSD to a less distorted electronic orbital configuration, Fe^{2+}-L to a more distorted one. The ΔE_Q of Fe^{2+} generally is temperature dependent via the valence-term contribution. Local electronic distortion environments with low deviation from cubic symmetry show large temperature dependence (Van Alboom et al. 1993). Looking on the temperature variation of the two Fe^{2+} sub-components between 80 K and room temperature (where electron delocalization plays a only minor role), we find the larger variation for Fe^{2+}-S, the one we propose to be the more regular one. In hedenbergite, only the regular Fe^{2+}-S orbital state does exist. As an aegirine component is substituted into hedenbergite, additional different local environments (due to Fe^{3+} and Na^+ neighbors) are established resulting in a group of more distorted orbital configurations. By increasing the aegirine content or by lowering the temperature, more and more Fe^{2+} can be found in this more distorted orbital state. At sufficiently low temperature (<80 K), only the Fe^{2+}-L state should exist. At sufficiently high temperature, only the Fe^{2+}-S is present. The latter has been demonstrated for the samples investigated here. The different compositional behavior of Fe^{2+}-S and Fe^{2+}-L can be explained by using the Ingalls (1964) model. As the Fe^{2+}-L is assumed to correspond to the more distorted LDE, it is in a range where the positive correlation between Fe^{2+} ΔE_Q and distortion is no longer valid but changes into a negative correlation, as it is usual for most minerals (Ingalls 1964; Dowty and Lindsley 1973).

Dollase and Gustafson (1982) summarized their interpretation of multiple models on page 326 by stating: "Nothing precludes there being in reality a large number of discrete states or simply a continuum of states." From the present research, it is concluded that there are not several states arising from discrete geometric NNN configurations, but that depending on the chemical composition there are two electronic distortion environments that are populated differently as a function of temperature. As already noted by De Grave et al. (1998), it remains unclear why the occurrence of distinct electronic configurations for Fe^{2+} in the same crystallographic site and the thermally induced gradual transformation between them seems to be restricted to Na-Ca clinopyroxenes. Similar to Amthauer and Rossman (1984), De Grave et al. (1998) suggested a second, alternative interpretation of the two Fe^{2+} components in natural aegirine: one of the two components participates in the electron hopping process. On the basis of the present data, such an interpretation cannot be excluded completely. Firm evidence can be given that there *is* thermally induced electron delocalization between Fe^{2+} and Fe^{3+} in the hedenbergite–aegirine solid-solution series starting above 250 K. This conclusion is based on the appearance of the additional QSD-site centered between the resonance absorption contributions of Fe^{2+} and Fe^{3+} at ~1.0–1.2 mm/s not mentioned by Amthauer and Rossman (1984) and De Grave et al. (1998). Following the alternative interpretation of De Grave et al. (1998), it is the Fe^{2+}-L component that probably could be influenced by the electron hopping process as its absorption area decreases as temperature rises. However, we have to note that even at low temperatures, two Fe^{2+} components are found, which would mean that, even at 80 K, one has to deal with thermally induced electron delocalization. This interpretation, however, is believed to be unrealistic. Further experiments on different Na-Ca solid-solution series, such as $CaFe^{2+}Si_2O_6$–$NaSc^{3+}Si_2O_6$, may help to find an answer to the problem of Fe^{2+} resonance absorption broadening in Na-Ca clinopyroxenes.

ACKNOWLEDGMENTS

G.J.R thanks the Alexander v. Humboldt-Stiftung for support during 1998–1999, when he was a Humboldt Fellow at the Institute of Crystallography at the RWTH Aachen. The basic ideas of this study and key experiments for single-crystal growth were worked out during that time. The study was supported financially by the Austrian Fonds zur Förderung der Wissenschaftlichen Forschung (FWF)

through grant R33-N10 (Erwin Schrödinger-Rückkehr-Stiprndium). Mr. Josef Ernst (RWTH Aachen) kindly helped us with the high-temperature/high-pressure experiments, and we thank him very much. The thorough reviews of F. Camara and an anonymous referee helped to increase the overall quality of the paper. Additionally, F. Camara is thanked for pointing out some structural relationships concerning the M1 and tetrahedral sites.

REFERENCES CITED

Aldridge, L.P., Bancroft, G.M., Fleet, M.E., and Herzberg, C.T. (1978) Omphacite studies, II. Mössbauer spectra of *C*2/*c* and *P*2/*n* omphacite. American Mineralogist, 63, 1107–1115.

Amthauer, G. and Rossmann, G. (1984) Mixed valence of iron in minerals with cation clusters. Physics and Chemistry of Minerals, 6, 19–30.

Bancroft, G.M. and Williams, P.G.L. (1969) Mössbauer spectra of omphacites. Mineralogical Society of America, Special Papers, 2, 59–69.

Burnham, C.W., Clark, J.R., Papike, J.J., and Prewitt, C.T. (1967) A proposed crystallographic nomenclature for clinopyroxene structures. Zeitschrift für Kristallographie, 125, 109–119.

Cameron, M. and Papike, J.J. (1981) Structural and chemical variations in pyroxenes. American Mineralogist, 66, 1–50.

Cameron, M., Shigehno, S., Prewitt, C.T., and Papike, J.J. (1973) High-temperature crystal chemistry of acmite, diopside, jadeite, spodumene, and urgeyite. American Mineralogist, 58, 594–618.

Clark, J.R., Appleman, D.E., and Papike, J.J. (1969) Crystal-chemical characterization of clinopyroxenes based on eight new structure refinements. Mineralogical Society of America, Special Papers, 2, 31–50.

De Grave, E. and Van Alboom, A. (1991) Evaluation of ferrous and ferric Mössbauer Fractions. Physics and Chemistry of Minerals, 18, 337–342.

De Grave, E., Van Alboom, A., and Eeckhout, S.G. (1998) Electronic and magnetic properties of a natural aegirine as observed from its Mössbauer spectra. Physics and Chemistry of Minerals, 25, 378–388.

Dollase, W.A. and Gustafson, W.I. (1982) ^{57}Fe Mössbauer spectra analysis of sodic clinopyroxenes. American Mineralogist, 67, 311–327.

Dowty, E. and Lindsley, D.H. (1973) Mössbauer spectra of synthetic hedenbergite-ferrosilite pyroxenes. American Mineralogist, 58, 850–868.

Eeckhout, S. and De Grave, E. (2003a) ^{57}Fe Mössbauer-effect studies of Ca-rich, Fe-bearing clinopyroxenes: Part I. Paramagnetic spectra of magnesian hedenbergite. American Mineralogist, 88, 1129–1137.

——— (2003b) ^{57}Fe Mössbauer-effect studies of Ca-rich, Fe-bearing clinopyroxenes: Part II. Magnetic spectra of magnesian hedenbergite. American Mineralogist, 88, 1138–1144.

Farrugia, L.J. (1999) WinGX suite for small-molecule single-crystal crystallography. Journal of Applied Crystallography, 32, 837–838.

Ingalls, R. (1964) Electric-field gradient tensor in ferrous compounds. Physical Reviews, 133, A787–795.

Litterst, F.J. and Amthauer, G. (1984) Electron delocalization in ilvaite, a reinterpretation of its ^{57}Fe Mössbauer spectrum. Physics and Chemistry of Minerals, 10, 250–255.

Ohashi, H. (2003) X-ray study on Si-O bonding. Maruzen Publishing Service, Tokyo.

Papike, J.J., Prewitt, C.T., Sueno, S., and Cameron, M. (1973) Pyroxenes; comparison of real and ideal structural topologies. Zeitschrift für Kristallographie, 138, 254–273.

Rancourt, D.G. (1994) Mössbauer spectroscopy of minerals I. Inadequacy of Lorentzian-line doublets in fitting spectraarising from quadrupole splittings distributions. Physics and Chemistry of Minerals, 21, 244–249.

Rancourt, D.G. and Ping, J.Y. (1991) Voigt-based methods for arbitrary-shape static hyperfine parameter distributions in Mössbauer spectroscopy. Nuclear Instruments and Methods in Physics Research B (NIMB), 58, 85–97.

Rancourt, D.G., McDonald, A.M., Lalonde, A.E., and Ping, J.Y. (1993) Mössbauer absorber thickness for accurate site populations in Fe-bearing minerals. American Mineralogist, 78, 1–7.

Rancourt, D.G., Christie, I.A.D., Royer, M., Kodama, H., Robert, J.L., Lalonde, A.E., and Murad, E. (1994) Determination of accurate $^{[4]}Fe^{3+}$, $^{[6]}Fe^{3+}$, and $^{[6]}Fe^{2+}$ site populations in synthetic annite by Mössbauer spectroscopy. American Mineralogist, 79, 51–62.

Rancourt, D.G., Ping, J.Y., Boukili, B., and Robert, J.L. (1996) Octahedral-site Fe^{2+} quadrupole splitting distributions from Mössbauer spectroscopy along (OH, F)-annite join. Physics and Chemistry of Minerals, 23, 63–71.

Redhammer, G.J. (1996) Untersuchungen zur Kristallchemie und Kristallphysik von synthetischen *C*2/*c* Klinopyroxenen im System Hedenbergit $CaFe^{2+}Si_2O_6$-Akmit $NaFe^{3+}Si_2O_6$, 199 p. Ph.D. thesis, University Salzburg.

——— (2001) Kontrollierte chemische Substitutionen in ausgewählten Ketten- und Schichtsilikaten: Beiträge von Mößbauerspektroskopie und Einkristall—Röntgenbeugung zu Kristallstruktur, Kristallchemie und Magnetismus von Glimmern und Klinopyroxenen. Habilitation Thesis, RWTH Aachen, 335 p.

Redhammer, G.J. and Roth, G. (2002) Structural variations in the aegirine solid-solution series $(Na,Li)FeSi_2O_6$ at 298 and 80 K. Zeitschrift für Kristallographie, 217, 1–10.

——— (2004a) Structural variation and crystal chemistry of $LiMe^{3+}Si_2O_6$ clinopyroxenes, Me^{3+} = Al, Ga, Cr, V, Fe, Sc, and In. Zeitschrift für Kristallographie, 219, 278–294.

——— (2004b) Structural changes upon the temperature dependent $C2/c \rightarrow P2_1/c$ phase transition in $LiMe^{3+}Si_2O_6$ clinopyroxenes, Me = Cr, Ga, Fe, V, and Sc. Zeitschrift für Kristallographie, 219(10), 585 – 605.

Redhammer, G.J., Amthauer, G., Treutmann, W., and Lottermoser, G. (2000) Synthesis and structural properties of clinopyroxenes on the hedenbergite $CaFe^{2+}Si_2O_6$-aegirine $NaFe^{3+}Si_2O_6$ solid solution. European Journal of Mineralogy, 12(1), 105–120.

Renner, B. and Lehmann, G. (1986) Correlation of angular and bond lengths distortion in TO_4 units in crystals. Zeitschrift für Kristallographie, 175, 43–59.

Robinson, K., Gibbs, G.V., and Ribbe, P.H. (1971) Quadratic elongation, a quantitative measure of distortion in coordination polyhedra. Science, 172, 567–570.

Rodrigues-Carvajal, J. (2001) Recent developments of the program FULLPROF. CPD Newsletter 26, 12–19; http://www.iucr.org/iucr-top/comm/cpd/Newsletters/.

Shannon, R.D. and Prewitt, C.T. (1969) Effective ionic radii in oxides and fluorides. Acta Crystallographica, B25, 925–934.

Sheldrick, G. (1997) SHELXS-97 and SHELXL-97, programs for solving and refining crystal structures. University of Göttingen, Germany.

Stoe and Cie (1996) X-SHAPE and X-RED: programs for optimizing of the crystal shape (w.r.t. the merging R-value) and numerical aborption correction. Stoe and Cie GmbH, Darmstadt, Germany.

Thompson, J.B., Jr. (1970) Geometric possibilities of amphibole structures: model biopyriboles. American Mineralogist, 55, 292–293.

Toraya, H. (1981) Distortions of octahedra and octahedral sheets in 1 *M* micas and the relation to their stability. Zeitschrift für Kristallographie, 157, 173–190.

Van Alboom, A., DeGrave, E., and Vandenberghe, E.R. (1993) Study of the temperature dependence of the hyperfine parameters in two orthopyroxenes by ^{57}Fe Mössbauer spectroscopy. Physics and Chemistry of Minerals, 20, 262–275.

Williams, P.G.L., Bancroft, G.M., Brown, M.G., and Turnock, A.C. (1971) Anomalous Mössbauer spectra of *C*2/*c* clinopyroxenes. Nature, Physical Science, 230, 149–151.

Wilson, A.J.C., Ed. (1992) International Tables for Crystallography, Volume C. Kluwer Academic Publishers, Dordrecht.

MANUSCRIPT RECEIVED NOVEMBER 29, 2005
MANUSCRIPT ACCEPTED MARCH 6, 2006
MANUSCRIPT HANDLED BY DARBY DYAR